UNIVERSITY OF CALIFORNIA,
IRVINE

Simple Methodology to Visualize Whole-Brain Microvasculature in Three Dimensions

THESIS

submitted in partial satisfaction of the requirements
for the degree of

MASTER OF SCIENCE

in Mathematical, Computational and Systems Biology

by

Katiana Marie Khouri

Thesis Committee:
Professor Bernard Choi
Professor Elliot Botvinick
Professor Anna Grosberg

2021

DEDICATION

To

My mother, father and son,
for all their sacrifices
to provide me with an
education, no matter the cost.

TABLE OF CONTENTS

LIST OF FIGURES

LIST OF TABLES

Page

ACKNOWLEDGEMENTS

I attribute my academic success to my mentor and committee chair, Dr. Bernard Choi. He has been a kind, and exceptionally wise guiding force on my path through graduate school. His humor and understanding made the hardest of lab days tolerable, and he encouraged us to enjoy our research. His capacity to indulge unconventional research proposals emboldened my confidence as an individual scientist and thinker. For these, I am eternally grateful

My committee members, Professor Anna Grosberg and Elliot Botvinick have embodied the family of support that is the Biomedical Engineering and Mathematical, Computational and Systems Biology (MCSB) community. They provided a platform for translational research and endless support to students, including myself, with the Edward's Life Sciences Cardiovascular Applied Research and Entrepreneurship (CARE) program. Without this funding and collaboration, I could not have competed my research or benefited from the countless resources. Thank you each for your time and contributions to my research.

I would also like to recognize the invaluable assistance from Drs. Adeela Syed, Sunil Gandhi, and Charless Fowlkes for their mentorship and research advice. They contributed to the formation of my research proposition and execution of innovative techniques requiring cross-discipline collaboration.

Lastly, I would like to thank my lab mates for their comradery and mentorship. Our incredibly supportive and adventurous lab culture kept graduate school apart from the mundane and made for some great memories. It would not have been the same without you!

To all of my teachers, and especially the "heart beat" of MCSB, Karen Martin, thank you for believing in me and navigating the waters ahead, no matter how tumultuous. Karen's persistence has been an unwavering force in the lives of many graduate students, especially myself, to which I will always be grateful.

ABSTRACT OF THE THESIS

Simple Methodology to Visualize Whole-Brain Microvasculature in Three Dimensions
by
Katiana Marie Khouri
Master of Science
in Mathematical, Computational and Systems Biology
University of California, Irvine, 2021
Professor Bernard Choi, Chair

Cerebral microbleeds characterize a heterogenous population of diseases responsible for serious brain injury and death. The current state of the field includes clarifying the origin and progression of microbleed associated diseases through identification of disease specific biomarkers and vascular contributors to hemorrhagic activity. Microbleeds have been associated with dysfunction of the microvasculature in several studies. While some vascular information can be gathered clinically (e.g. through magnetic resonance imaging, MRI), identification of capillary level information requires the use of ex-vivo analysis. While the current standard is 2D histology of thin (e.g. 40 micron) brain sections, progression of research in this field may benefit from a tool to represent microbleeds and surrounding vascular structure systemically in the whole, unaltered organ.

To explore brain architecture and pathology, a consistent and reliable methodology to visualize the three-dimensional cerebral microvasculature is beneficial. Perfusion-based vascular labeling is quick and easily deliverable. However, the quality of vascular labeling can vary with perfusion-based labels due to aggregate formation, leakage, rapid photobleaching, and incomplete perfusion. Here, we describe a simple, two-day protocol with perfusion-based

labeling that facilitates whole-brain, three-dimensional microvascular imaging and characterization. The combination of retro-orbital injection of Lectin-Dylight-649 to label the vasculature, the clearing process of a modified iDISCO+ protocol, and light-sheet imaging, collectively enables a comprehensive view of the cerebrovasculature. We observed an ~18-fold increase in contrast-to-background ratio of Lectin-Dylight-649 vascular labeling over endogenous GFP fluorescence from a transgenic mouse model. With light-sheet microscopy, we demonstrate sharp visualization of cerebral microvasculature throughout the intact mouse brain. Our tissue preparation protocol requires fairly routine processing steps and is compatible with multiple types of optical microscopy.

Further, machine learning techniques provide an advantage to large data sets which may apply to the delineation of vascular structures. To test this theory, we use deep learning algorithms on vascular images taken by our lab of cleared whole organs labeled with Lectin Dylight and imaged with lightsheet microscopy. Convolutional neural networks (CNNs) via transfer learning were used for the multi-class classification of mouse organs from vasculature images. The datasets were put through multiple CNNs pre-trained on ImageNet including GoogLeNet, Inceptionv3, and NASNetLarge. Among them, GoogLeNet was the best because of the high accuracy among training and test datasets and relatively quick prediction rate.

INTRODUCTION

The complex vascular network supplies the brain with necessary metabolites and oxygen. Dysfunction of the cerebral microvasculature is associated with several disorders, including schizophrenia, traumatic brain injury, dementia, and stroke.[1,2,3] However, the role of microvasculature in the development of cerebral disorders remains ambiguous despite implications in ~45% of dementia cases and ~20% of strokes.[1]

Cerebral Microbleeds (MBs) in the brain, which can result from chronic brain injury, inflammation, hypertension, chronic obstructive pulmonary disease or several other pathologies, are likely caused by structural abnormalities of the cerebral microvasculature.[4] However, diseases associated with MBs are varied and heterogeneous in their pathophysiological descriptions. Deciphering the MB environment and potentially identifying biomarkers indicative of disease burden would aid in the discovery of prevention and treatment strategies.[5] While MRI is used clinically to detect and diagnose MB burden, it does not allow for association to cellular changes to distinguish its pathological origin.[5] Thus, ex vivo analysis is useful in depicting microvascular pathology of MBs.

Currently, pathological studies are conducted using traditional histological methods on thin brain sections, which are used to extract 3D representations.[4,5] MBs are identified through labeling of hemosidrin, which is a biproduct of the blood degredation deposited after a bleed occurs.[4] Prussian blue in conjunction with hematoxylin and eosin (H&E) staining are used to label the hemosidrin deposits and assess MB burden (Figure 1).[4]

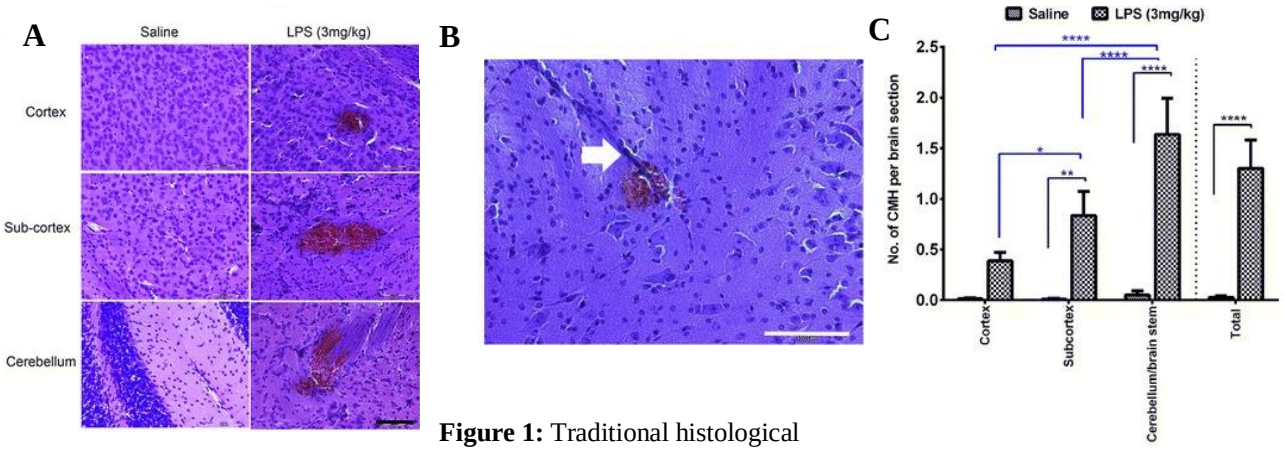

Figure 1: Traditional histological identification of microhemorrhages with H&E staining of 40-µm coronal sections by Rachita Sumbria, UCI (2016).[4] (A) Microhemmorhages induced under an inflammatory model with lipopolysaccharide (LPS) (B) Representative images of (A) including blood vessel identification in association with mirohemorrhage. (C) Significant differences in regional microhemmorhage burden. Scale bar = 100 µm.

Currently, two- dimensional histology is considered the gold standard for obtaining micron-resolution vasculature images.[6,7] However, in addition to its laborious nature, standard histological sections, often 40µm thick, are prone to artefacts and difficult to use for full organ re-construction.[8, 6] Imaging thicker tissues faces the obstacles of overcoming highly scattering tissue and enhancing the visibility of vasculature. Optical histology, a technique developed by our lab, expands two-dimensional histology to thicker tissue sections with tissue clearing and vascular labeling.[13,8] Combining these techniques increased imaging depth and improves vascular density quantifications.[8]

Vascular labeling techniques include secondary antibody staining via diffusion, transgenic endothelial markers, and vessel painting perfusion-based methods. While secondary antibody staining requires long labeling periods (up to weeks)[9], and transgenic mouse models require breeding time[11], perfusion-based vascular labeling is quick and easily deliverable[11,12,13].

However, the quality of vascular labeling can vary with perfusion-based labels due to aggregate formation, leakage, rapid photobleaching, and incomplete perfusion[11,14,15,16].

Perfusion administered vessel painting agents can be distinguished by their selective cell binding sites and solubility. For example, Lycopersicon Esculentum Lectin (Lectin), a glycoprotein with a binding affinity to glycoprotein moieties found in the vascular endothelium, has derivatives including Fluorescein Isothiocyanate (FITC) and Dylight-649, which are lipophobic. DiI-C18 is a lipophilic carbocyanine fluorescent dye that embeds itself in the lipid membrane of cells.[14]

Lectin-FITC has been used to label vasculature, in combination with 3DISCO[12] and CLARITY optical clearing protocols[17]. However, the FITC conjugate is limited by quick photobleaching, sensitive fluorescence dose dependence, and hydrophobicity making it incompatibile with organic solvents.[18] Similarly, DiI-C18, may be susceptible to aggregate formation during perfusion and is not compatible with organic solvents.[14] Conversely, the newer Lectin-Dylight derivatives are hydrophillic, compatible with organic solvents and more stable.[15]

Our lab has established perfusion based vascular labeling techniques capable of providing high resolution identification of microscopic vessels that withstand clearing methods.[13,8] To determine the best vascular label, we assessed the three vessel painting agents: (A) DiI-C18, (B) Lectin-FITC, and (C) Lectin-Dylight649. We experimentally compared the capabilities and limitations of each of these three agents in the following pairs: (1) DiI-C18 (ThermoFisher Scientific D-282, Waltham, MA) with Lectin-FITC (Sigma Aldrich L0401, Burlington, MA) and (2) DiI-C18 with Lectin-Dylight649 (Vector Laboratories DL-1178, Burlingame, CA) (Figure 2).

While DiI tended to label large vasculature with high contrast, the large conjugate visibly reduced diffusion into smaller capillaries. The diffuse staining of Lectin-FITC precluded identification of key vascular structures. However, we found Lectin-Dylight to label both the macro and microvascular structures consistently.

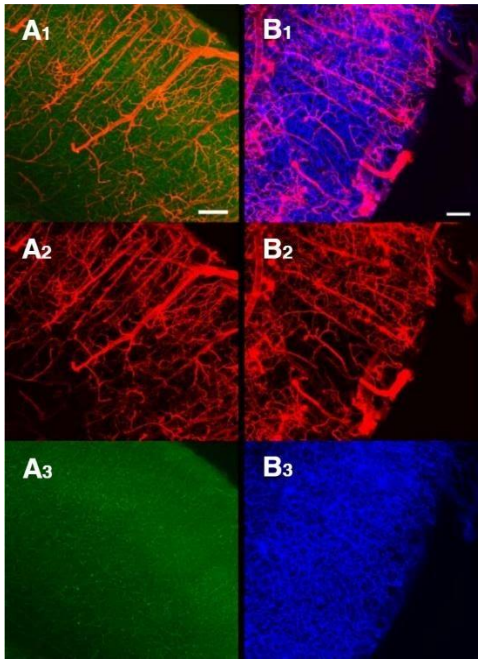

Figure 2: Perfusion vessel painting comparisons with maximum intensity projections performed by our lab member, Adrian Bahani. (A1) DiI-C18 and Lectin -FITC overlay image. Scale bar 150 µm. (A2-3) DiI-C18 and Lectin-FITC painted vasculature, respectively. B1) DiI-C18 and Lectin -Dylight-650 overlay. Scale bar 125 µm. (B2-3) DiI-C18 and Lectin -Dylight650 painted vasculature, respectively.

Tissue clearing techniques enable cellular and subcellular resolution on a systemic scale by rendering the tissues transparent. Optical clarity is achieved through one of three main approaches: hydrophobic (solvent), hydrophilic (aqueous) and hydrogel methods.[7] The first two reduce tissue scattering and light absorption significantly through extraction of lipids, pigments and calcium compounds in conjunction with refractive index (RI) matching of imaging solution and specimen.[7] Hydro-gel processes use a synthetic gel structure to hold the molecules in place

while uniformly removing lipids and passively diffusing biomolecular labels, although passive diffusion requires long incubation times. [7]

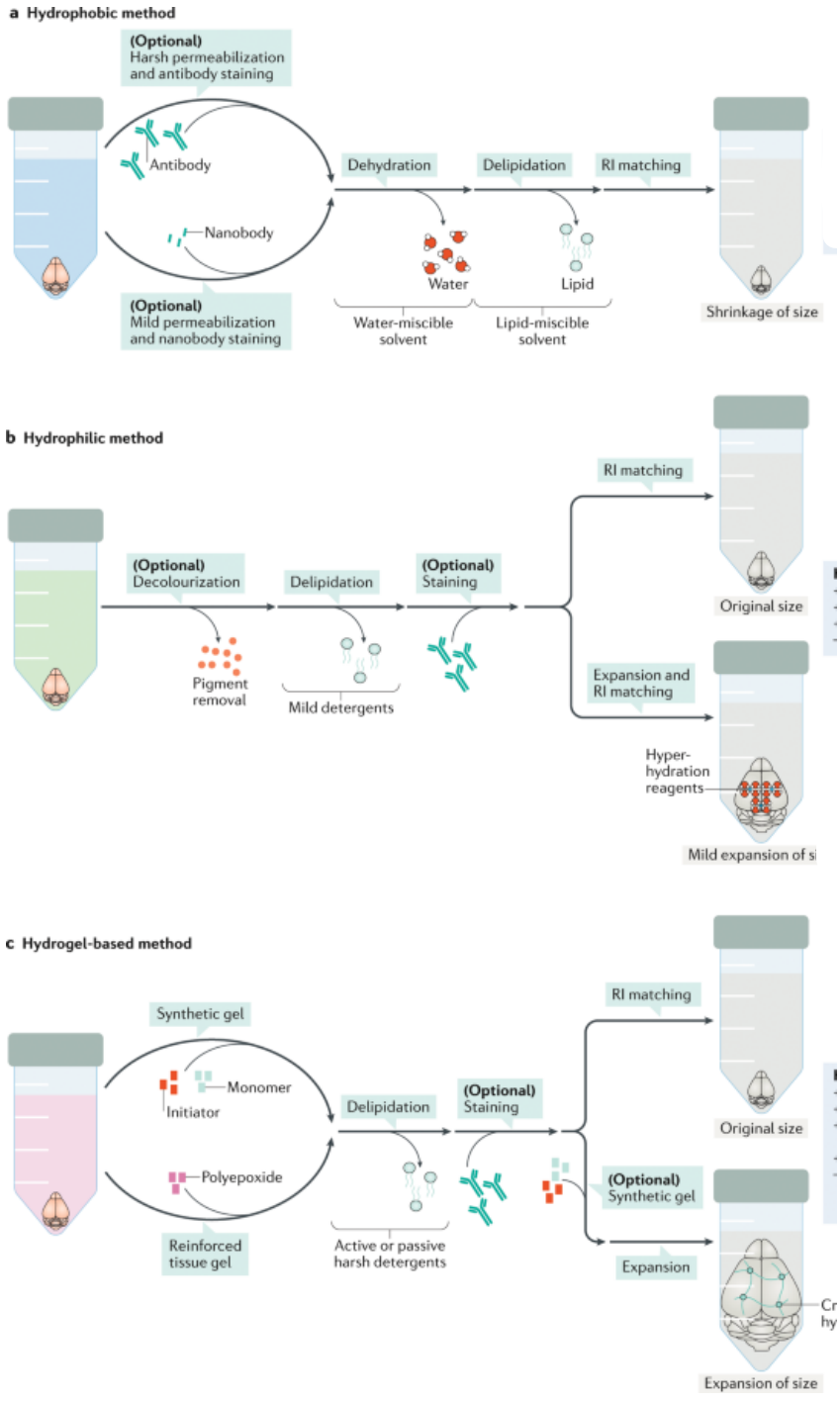

Figure 3: Comparison of Three major clearing categories adapted from Ueda et al., 2020 [7]. (A) Hydrophobic techniques (e.g. DISCO) remove, water, lipids, match refractive index (RI) and result in tissue shrinkage. (B) Hydrophilic processes remove, color, lipids, introduce staining. (C) Utilize a structural gel, removes lipids, introduces stain and (B&C) use RI matching and can result in expansion.

Hydrophobic processes include the DISCO methods, which rely on dehydration and consecutive emersions in organic solvent solutions for delipidation, leaving biological tissues and an organic solvent solution with similar RIs ~1.56.[9,7] There have been several variations on the DISCO process including uDISCO, iDISCO and vDISCO, the latter of which is the most recent attempt to increase compatibility with large chain antibodies for immunostaining in the whole mouse body. [7,10]

Hydrophilic procedures include See Deep Brain (SeeDB), CUBIC, FocusClear, and Sca*l*e, which utilize aqueous environments and can cause sample expansion through hyperhydration. In contrast to hydrophobic methods, hydrophilic processes tend to reduce RI.[7,19] They often require longer incubation periods, although biocompatibility is increased and can allow for increased fluorescence preservation. [7,20] Expansion on this technique has made hydrophilic procedures contenders with the usually faster and easier hydrophobic processes and support such movements as the CUBIC Atlas, a 3D single cell resolution mouse brain map. [7,21]

Hydrogel processes work through creating covalent linkages to an acryl-based hydrogel followed by delipidation.[7] An example of which is cleared lipid-extracted acryl-hybridized rigid immunostaining/in situ hybridization-compatible tissue hydrogel' (CLARITY).[22] This method had since been expanded upon to increase macromolecule permeability in the gel for

immunolabeling with conservation of organ shape and biomolecules including passive CLARITY technique (PACT) AND Stochastic electrotransport.[7,23,24,22]

Tissue clearing procedures have progressed rapidly and now enable whole-organ clearing using the aforementioned techniques[,25,26]. Incorporating light-sheet microscopy (LSM) has reduced whole-organ imaging time (~1-2 hours) while maintaining microscopic resolution and mitigating photobleaching[27]. Recent reports demonstrate whole-organ vascular visualization in the brain and teeth[25,28]. However, the use of complicated clearing procedures necessitating lengthy labeling techniques and non-standard equipment has precluded the routine use of these methodologies for scientific research[11,17]. While the use of thicker cleared sections in optical histology allowed for improved visualization of three-dimensional structures,[8] we anticipate that whole organ clearing will further alleviate the limitations of two-dimension histology by eliminating slicing altogether. To our knowledge a systemic technique to identify microbleed burden in the whole brain does not currently exist.

Fundamental to exploring these relationships is a consistent and reliable methodology to visualize the three-dimensional cerebral microvasculature under normal and pathological conditions. The advantage of whole-organ modeling and computational representations of key anatomical structures for use in research and clinical applications has been realized by several universities and companies.[9,29,30] However, ability to image whole-organs at once and obtain micron resolution images has been limited. Researchers would benefit from whole-brain models of the cerebrovascular structure. The crucial and challenging task of creating useful whole-organ

visualizations requires the pairing of compatible labeling, clearing, and imaging techniques using repeatable and robust methodologies and equipment.[31]

Here, we describe a simple, two-day protocol with perfusion-based labeling that facilitates whole-brain, three-dimensional microvascular imaging and characterization. We anticipate that this approach can be used to study the relationship between microvascular structure and function with cerebral pathology and to fit mathematical models of hypoxia predictive of ischemic conditions in the brain. Our lab's goal is to develop three-dimensional, high resolution, whole-brain maps of the cerebral microvasculature. This will address the knowledge gap surrounding vasculature changes during disease progression and ultimately support the development of innovative treatment paradigms.

Further, in anticipation of future directions of large data image analysis, we are interested in testing the capacity of machine learning techniques to detect and categorize vascular structures. Previous literature shows that classification problems involving vessels are commonly approached with segmentation. Badawi and Fraz created a deep encoder-decoder convolutional neural network (CNN) to segment retinal vessels and classify them as either arteries or veins.[32] Segmentation is the mapping of vessels and subsequent characterization that may allow for features unique to vessels to be processed by the CNN. Similarly, Haft-Javaherian et al. created a CNN dedicated to vessel segmentation called DeepVess and applied the system to study vasculature in Alzheimer disease mouse models.[33] Furthermore, Montoya et al. devised a CNN that could recreate the 3D vascular anatomy of the image using a single contrast-enhanced CT acquisition through the classification of image voxels into vasculature, bone, and soft tissue.[34]

Based on the aforementioned work, segmentation appears to be important in classification problems involving vasculature images. However, the work by Montoya et al[34] work shows the possibility of classification using a deep CNN without preprocessed segmentation.[34] Thus, my aim was to explore the use of a CNN that can classify organs based on their vasculature without explicit segmentation.

MATERIALS AND METHODS

Preliminary Data:

Exogenous Fluorescent Dyes

Dye Compatibility plays an important role in the viability of clearing with organic solvents. Since organic solvent clearing methods rely on the removal of lipids to achieve clarity, lipophilic clearing methods are not compatible with them. A preliminary test of the compatibility of DiI vessel labeling with iDISCO+ supports this hypothesis, with visual leakage of dye into the solvent (Methods Figure 1A). Conversely, use of Lectin-Dylight-649 showed no obvious leakage visually, as demonstrated midway through the final clearing stage of DBE submersion (Methods Figure 1B).

Prussian Blue (PB), an important component in microbleed detection, was tested on spleens due to the prevalence of hemosiderin in these organs. After submersion, the spleens showed obvious, prevalent staining by PB. After exposure to the iDISCO+ procedure, the spleens showed no

visual signs of dye leakage and the stain appeared to remain within the organ (Methods Figure 1 C and D).

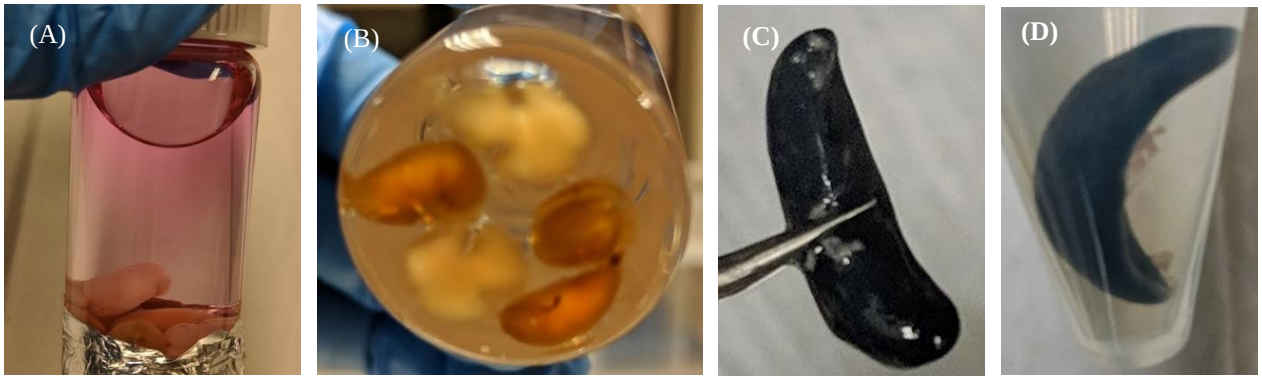

Methods Figure 1: Experimental determination of iDISCO+ compatibility with stains. (A) DiI-C_{18}, stained organs leaking dye in the DCM washes. (B) A snapshot of multiple organs, two brains, two kidneys and a heart, fifteen minutes into DBE submersion labeled with Lectin-Dylight-649. (C) A spleen labeled with Prussian blue staining before any clearing processing. (D) Spleen post clearing immersions with clear appearing liquid and blue stain intact.

Prussian blue stained microbleeds are visible when cleared with iDISCO+ methodology. Previously, our lab compared simple one-step immersion clearing protocols utilizing the same microscope, (Nuance, PerkinElmer), on 1mm thick brain slices.[35] Additionally, PB staining of microbleeds has been done in our lab and in collaboration with the Fisher and Cribb's labs.[4] Combination of these techniques revealed visual compatibility of microbleed labeling with organic solvent clearing procedures (Methods Figure 2). In contrast, submersion in FocusClear (CelExplorer, Taiwan), led to disappearance of dye entirely in positive control microbleed brains (data not shown). PB compatibility with iDISCO+ clearing procedures in 500 μm slices suggests

an opportunity for extension of whole organ microbleed mapping without tissue slicing, utilizing these two techniques.

To further delineate the potential of for whole-organ imaging, the 500 μm slices were mounted either on a cover slip or capillary (Methods Figure 2 C/D). Light-sheet microscopy of these samples revealed visibility of PB stained microbleeds (E). Additionally, comparison of brightfield and transmission microscopy (638nm) showed overlap of microbleed visibility with vascular labeling (Methods Figure 2 F/G). While brightfield images easily identify microbleeds, 638nm images reveal vasculature and some visibility of microbleeds concurrently. Light-sheet microscopy of vascular and PB labels concurrently suggests utility of this technique to study pathological characteristics systemically.

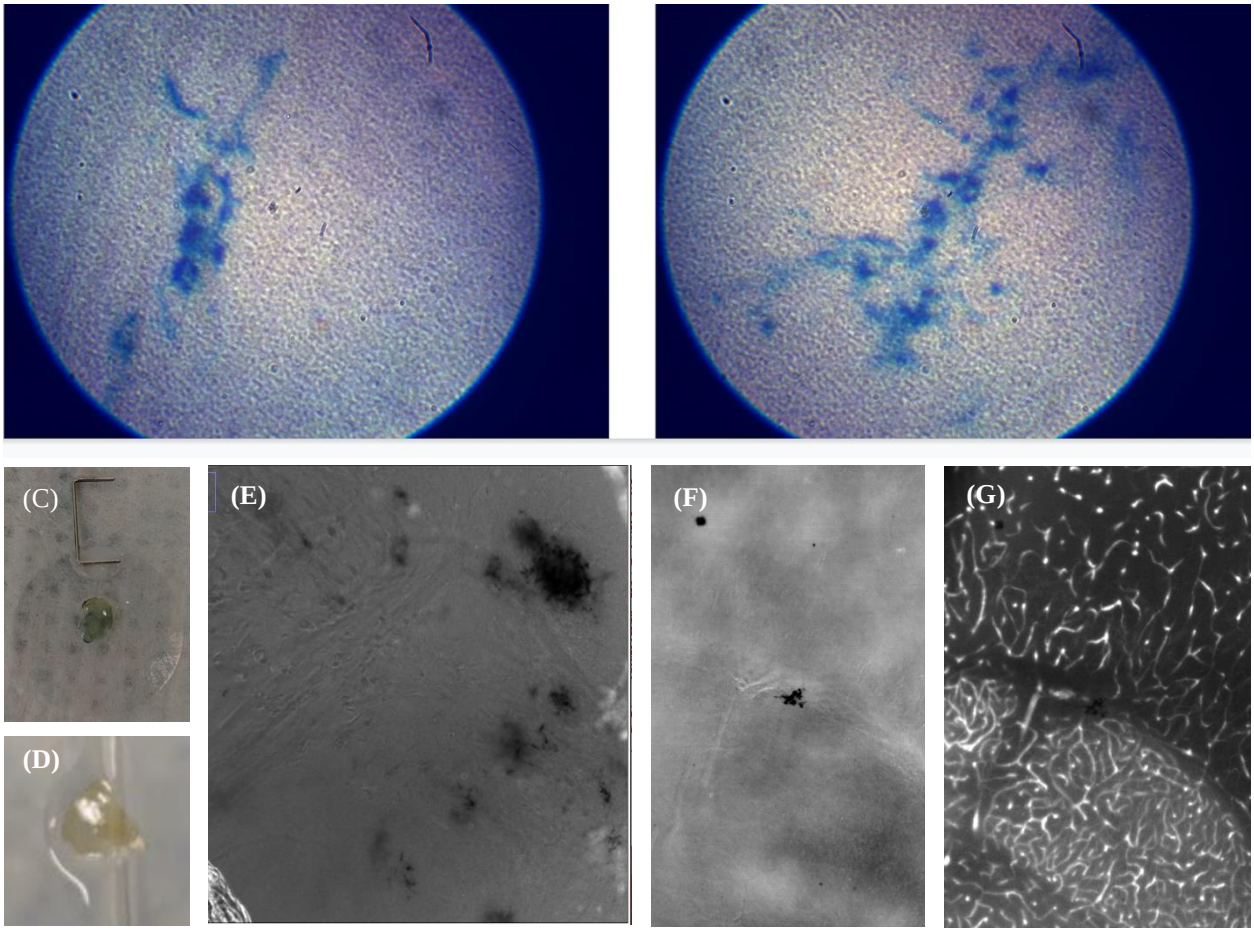

Methods Figure 2: Assessing visibility of Prussian Blue stained 500-µm brain tissue slices cleared with iDISCO+. (A/B) using our labs standard Nuance microscope. (C/D) Two preparations of slice mounting for light sheet imaging: mounted on a coverslip or capillary, respectively, with epoxy. (E) 500 µm brain slice mounted on the coverslip (C) from the light sheet (snapshot of one z-stack) . (F/G) Brightfield and 638nm excitation single z-stack image of coverslip-mounted slice.

The vasculature of other organs is visible using our lectin labeling method and iDISCO+ protocol. The systemic administration of Lectin Dylight-649 allowed us to probe its utility with iDISCO+ clearing to visualize microvessels in other organs. Clearing and imaging the bladder, kidneys, uterus and heart revealed the unique microvascular structures in each organ (Methods

Figure 3 C/F/G/H). The cleared organs appeared translucent (Methods Figure 3 A/B). Inspection of bladder vasculature image reveals vessel detail on several scales (Methods Figure 3 C/D/E).

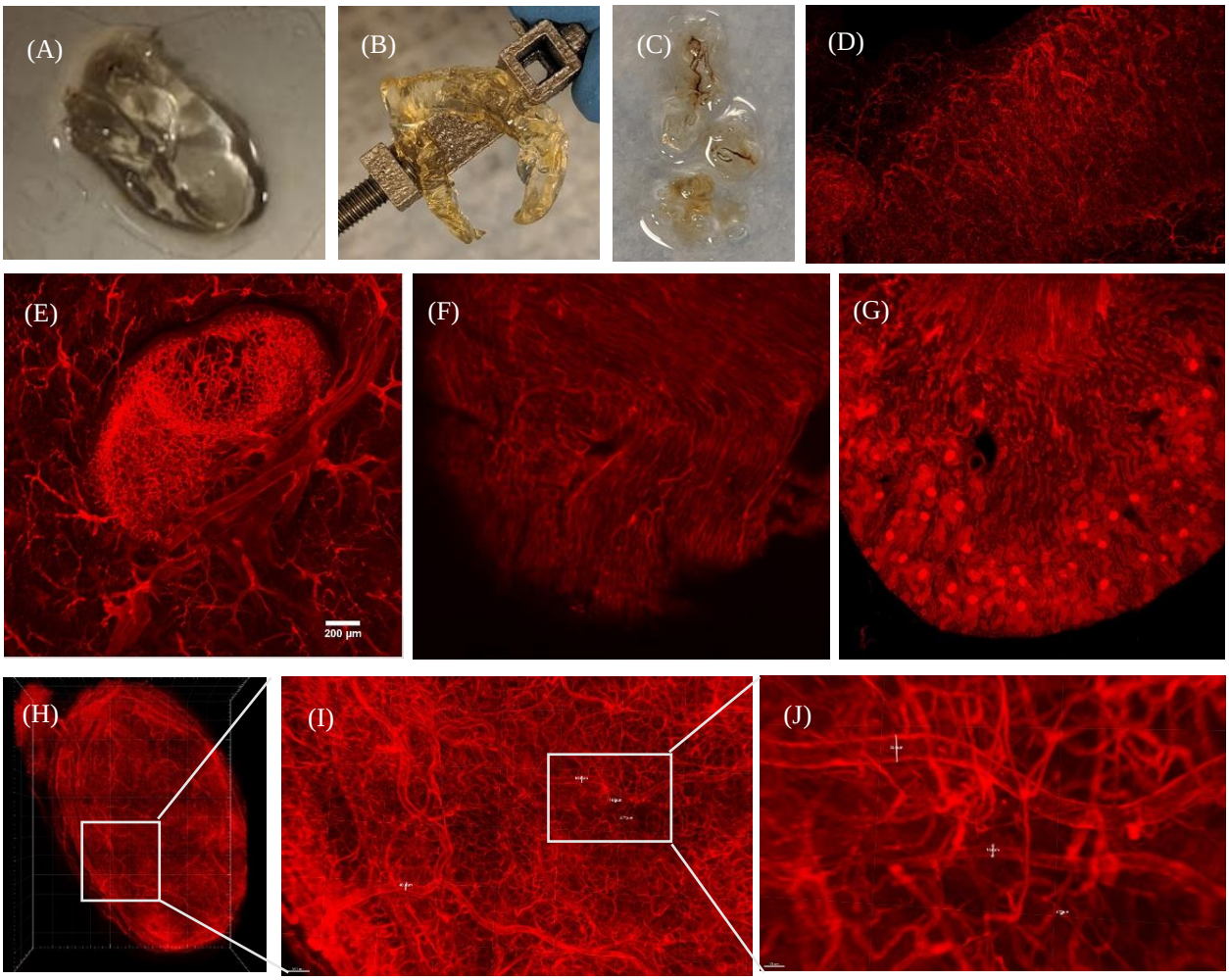

Methods Figure 3: Extending whole-organ clearing to the bladder, uterus, kidneys, lymph nodes and heart with Lectin Dylight-649 and iDISCO+ clearing. (A) Cleared bladder mounted on thin cover glass with epoxy ring of DBE. (B) Uterus mounted and secured with a screw for imaging in the light sheet chamber. (C) Cleared lymph nodes on a cover glass in DBE. (D-J) Maximum intensity projections (MIP) of various organs (D) Uterus (E) Mammary Gland lymph node (F) Heart (G) Kidney (H-J) Bladder with inlet magnifications.

With completion of these preliminary methodology steps, we then set out to perform more detailed analysis of cerebral vasculature.

Experiments:

Animal models

All animal experiments were performed under a protocol approved by the Institutional Animal Care and Use Committee at the University of California, Irvine. Whole-brain vessel painting experiments were performed using an adult transgenic mouse model (*Tie2-GFP)* expressing Green Fluorescent Protein (GFP) in vascular endothelial cells (Tg (TIE2-GFP)287Sato/J Stock No: 003658 Jackson Laboratory, Bar Harbor, ME) (n=4).

Vessel Painting

For all mice, anesthesia was performed using 5% isoflurane inhalation followed by IP administration of a ketamine-xylazine cocktail (90 mg/kg ketamine, 10 mg/kg xylazine). A diluted aliquot (50 μL dye, 150 μL saline) of Lectin Dylight-649 was administered via retro-orbital injection. The dye was allowed to circulate for 30 min, followed by an IP injection of euthasol (195 mg sodium pentobarbital). Cardiac perfusion of 10 mL saline followed by 10 mL of 10% formalin was immediately performed to flush out the blood and fix the tissue, respectively.

Brain Extraction

After vessel painting, the brains were harvested and immersed in 10% formalin for 24 hours in the dark, then transferred to a 0.1% sodium azide solution (balance PBS) and stored at 4°C.

Prussian Blue Microbleed Labeling

First, a solution of Potassium Ferrocyanide Trihydrate Solution (PFT) was made to be used in a working solution in one of two 100 mL glass containers (bottles or beakers are fine).
Ten g of PFT was measured out with a metal spatula and poured into an empty 100 mL glass container. A graduated cylinder was used to collect about 100 mL deionized water (DIW) which was poured into the glass with PFT until it reached 100 mL of volume. A magnetic stirring rod was added into the glass container and the container placed on the magnetic stir plate and turned on. The solution was allowed to mix for at least 10 minutes (Methods Figure 4A), until the PTF was fully dissolved.

Second, the HCL Solution was made (20%) by measuring 80 mL of DIW in a graduated cylinder and poured into a 100 mL glass container. From the HCl bottle (Fisher Scientific, A144-212), a pipette controller with 10 mL pipette tip was used to transfer 20 mL of HCl into the glass container that contained 80mL of DIW.

Third, the samples were washed. As samples contained lectin, a photosensitive compound, light exposure was kept to a minimum. A secondary waste container (beaker) was used for collecting the sodium azide solution within which the samples were stored. A graduated cylinder was used to collect DIW, filled to approximately half the volume of the vial (10mL). The samples were submerged in the vials with DIW. The vial was placed on a rotating device for 5 minutes at a speed setting of 4 (Methods Figure 4B). The DIW inside of each vial was poured out and the samples were submerged in 95% ethanol, which was approximately half the volume of the vial

(Methods Figure 4C). The vial was placed on a rotating device (e.g. nutator) for 5 minutes. The 95% ethanol inside of each vial was poured into a secondary waste container. Samples were submerged in DIW, approximately half the volume of the vial. Vials were placed on the rotating device and left as the working solution was made (next step).

Fourth, the working solution was made (1:1 ratio of the PTF and 20% HCl solution). Inside the fume hood, a 50 mL pipette tip and gun was used to pipette 100 mL of PTF into empty glass beaker (Methods Figure 4D). Then, the pipette was used to place 100 mL of 20% HCl solution into the same beaker. Importantly, the working solution was mixed by shaking beaker to ensure it was mixed properly.

Fifth, the samples were submerged in the working solution. The DIW was poured out of each vial and working solution (approximately half vial ~10 mL) added in its place. The vial was left on the rotating device for 1 hour for a 1mm thick brain slice. The working solution was poured out from each vial into a secondary waste container. Then, each sample was submerged in DIW for 5 minutes on the rotating device. The DIW was poured out and resubmerged in DIW again. Finally, the samples were stored in a dark refrigerator. An example PB stain is shown in Methods Figure 4E.

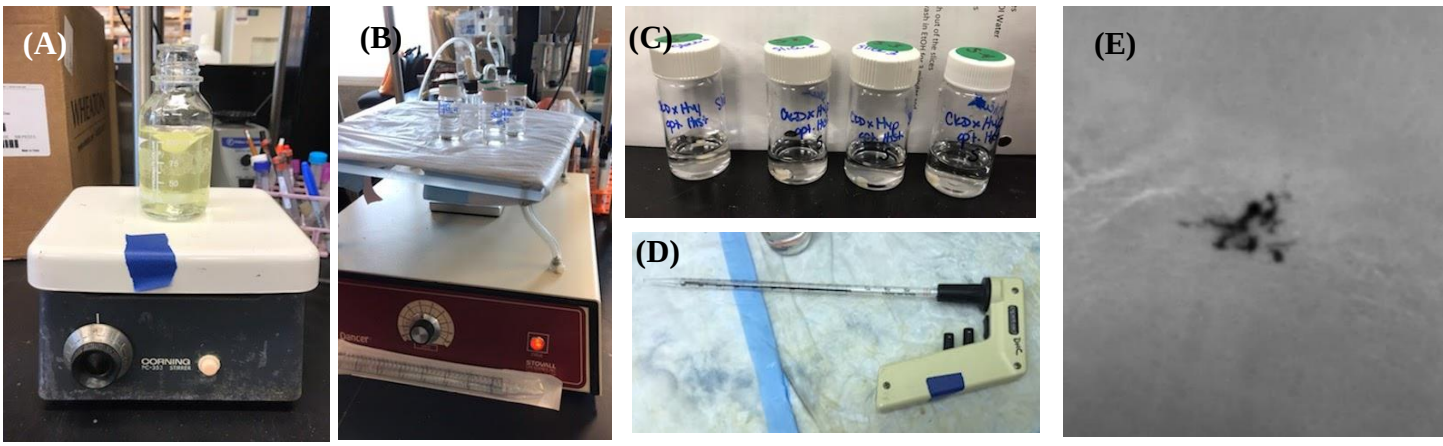

Methods Figure 4: Prussian Blue labeling process for 1mm murine brain slices. (A) PFT solution stirring with magnetic rod on the stir plate. (B) nutator utilized for slow mixing of solutions. (C) Example brain hemispheres in half filled vials of solution. (D) Pipettor gun for extracting solutions. (E) Example microbleed stained through PB protocol.

Tissue Clearing

Whole organ: We modified the published iDISCO+ protocol[9] to achieve whole-brain clearing in two days with one round of dehydration and elimination of the secondary antibody labeling procedures. Samples were dehydrated with a cascading methanol treatment (20%, 40%, 60%, 80%, 100%, 100%, balance sterilized water) for one hour each at room temperature (Table 1). Stock solutions of each methanol/de-ionized water were created the day of (to avoid degradation) in large tubes. The samples were placed on a nutator for each mixing period. During this treatment, samples were placed in 5ml black Eppendorf tubes to avoid potential photobleaching effects of ambient light. After the last 100% immersion, samples were placed on a nutator and allowed to mix overnight. They were then submerged in 66% dichloromethane (DCM) (Sigma 270997-12X100ML) (balance methanol) for three hours and left on the nutator to mix. The 1/3 methanol was first added to the Eppendorf tube with the sample in it. The DCM was in an

airtight bottle to prevent oxygenation. A syringe was used to retrieve the liquid while in the hood. The bottle was turned upside down to withdraw liquid, ensuring a syringe compatible with DCM is used for transfer. Two 15-minute washes of 100% DCM were done to remove excess methanol. The samples were submerged in dibenzyl ether (DBE) (Sigma 108014-1KG) and kept in the dark until imaging, keeping as much air out of the containers as possible to prevent oxidation. Tissue clarity should occur after 20 minutes to 2 hours of DBE immersion.

Container Number	% methanol	Volume methanol	Volume D.I.H20	Total Volume
1	20	900**µ**L x 2 = 1800 **µ**L	900**µ**L x 8 = 7200 **µ**L	9000 **µ**L
2	40	900**µ**L x 4 = 3600**µ**L	900**µ**L x 6 = 5400 **µ**L	9000 **µ**L
3	60	900**µ**L x 6 = 5400 **µ**L	900**µ**L x 4 = 3600**µ**L	9000 **µ**L
4	80	900**µ**L x 8 = 7200 **µ**L	900**µ**L x 2 = 1800 **µ**L	9000 **µ**L
5	100	900**µ**L x 10 = 9000 **µ**L	0 **µ**L	9000 **µ**L

Table 1: Dilution calculations for iDisco+ dehydration methanol washes for 5 tissue samples to be cleared.

Microscope comparison: Sections were cleared with a shortened version of the whole-organ modified iDISCO+ clearing protocol, with methanol and DCM immersions lasting 1/3 of the time. Thus, each methanol submersion lasted 20 minutes, and DCM an hour (Table 2).

	Methanol dilutions: (20%, 40%, 60%, 80%, 100%, 100%)	66% DCM / 33% Methanol	100% DCM	DBE
Whole organ	1 hour each	3 hours	15 minutes	> 2 hours
1mm sliced tissue	20 minutes each	1 hour	5 minutes	> 20 minutes

Table 2: Immersion times for whole or sliced tissue samples. Tissue sample container is drained and refilled with the appropriate consecutive solution.

Imaging

Comparison of Tie2-GFP endogenous and Lectin-Dylight-649 exogenous fluorescence: Spectral images were acquired with the Leica True Confocal Scanner SP8 (Leica Biosystems, Il., US) with a 10x/.3 NA HC PL Fluotar objective. Brains were imaged by collecting 52 z-slices, each 10 μm thick, of 1024x1024 images at an excitation of 488 nm and 633 for Tie2-GFP and Lectin-Dylight fluorescence, respectively.

Microscopy comparison: Slices were imaged with the above LSM (~1.14 micron resolution) and confocal LSM 980 Airyscan (airyscan) (~0.1 micron resolution). The slices were mounted in the LSM using a capillary tube and epoxy glue then followed the imaging protocol above for whole-brain. The airyscan, with an area detector of 32 concentrically arranged detection elements, was used with the 639 nm excitation laser and 655-750nm emission detector. A Z-stack (1824x1824 pixel: 177.9x177.9 μm) image was collected of 41 slices each 0.15 μm thick at 2.4x.

Whole-brain and whole-heart rendering: An LSM (Z.1, Zeiss) equipped with an s-CMOS PCO.edge camera and two perpendicular objectives for excitation and detection, was used to image the whole brain. The sample was submerged in DBE in a custom chamber (Translucence, San Diego, CA) and suspended from a custom organ holder. The 5x/0.16 (NA) imaging objective was used with 638 nm and 488nm excitation lasers with 640nm and 490nm BP filters for Lectin-Dylight and autofluorescence, respectively. Z-stacks (2652x2652 pixel) of 849 slices, each 5.84 μm thick, were acquired for each tile. Multiple tiles were collected with a 20% overlap among tiles to facilitate subsequent image stitching.

Micro-hemorrhage and vascular co-localization: Spectral images were acquired with the Leica True Confocal Scanner SP8 (Leica Biosystems, Il., US) with a 10x/.3 NA HC PL Fluotar objective. Brains were imaged by collecting 167 z-slices, each 7.63 μm thick, of 1750.6x1750.6 images at an excitation of 633 for Lectin-Dylight fluorescence. Multiple tiles were collected with a 20% overlap among tiles to facilitate subsequent image stitching.

Image Processing

Comparison of Tie2-GFP endogenous and Lectin-Dylight-649 exogenous fluorescence: MIPs of the two-channel images were made for cross-comparison. One hundred ROIs were manually selected with the rectangular shape tool in FIJI (Version 1.52p, National Institutes of Health, https://imagej.net/Fiji) with the ROI manager and image overlay functions. Vascular regions were selected in clearly visible vessel regions in the higher contrast lectin channel and the co-registered fluorescence emission from the Tie2-GFP channel analyzed.

Whole-brain and whole-heart rendering: Tiles were manually sorted and stitched with Arivis Tile Sorter (Vision 4D, Arivis AG, Munich, Germany), then saved and converted using the Imaris File Converter (9.3.1, Bitplane, Oxon, UK). Imaris was used to create whole-brain renderings of the cerebrovasculature. Shading was done with the "blend" feature to show surface level vasculature and "normal shading" to show more internal structures. FIJI was used to create maximum intensity projections (MIPs) and for single-slice visualization of vasculature.

Micro-hemorrhage and vascular co-localization: Tiles were stitched during collection by the Leica SP8 software. Subsequently, the tiles were loaded into FIJI for extraction of microbleed coordinates, which were saved as a text document. Tiles were separately loaded into *Neutube* (Howard Hughes Medical Institute, Janelia Research Campus, Ashburn, VA 20147) and traced with coordinates saved. Microbleed and vascular coordinates were loaded into MATLAB (1994-2020 The MathWorks, Inc., R2019a) for visualization.

Data Analysis

Contrast-to-background ratio (CBR) was calculated as the quotient of the mean fluorescence emission of the vascular ROIs and that of the perivascular background ROIs. All statistical analyses were performed with Prism software (Version 8, GraphPad Software, LLC). A Kruskal-Wallis test with multiple comparisons was used to compare lectin-Dylight-649 and GFP emission from vascular and background regions. Significance level was set at $p=0.05$.

Machine Learning Techniques

Data: As an initial test, images of kidney, heart, brain, uterus, mammary gland and lymph node were used to test the ability of image analysis algorithms (see next section) to distinguish vascular organ origin. The data was loaded as separate tiles given their size for input into the learning algorithms. Each tile is a .czi file composed of a z-stack of approximately 500 slices and dimensions of 1024x1024. Fluorescence of the 649 nm excitation label was achieved with a 638 nm laser and 640 nm emission filter with a magnification of 5x.

Image Processing: The data were first preprocessed with FIJI (version 1.52p, NIH, Bethesda, Maryland) to separate tiles and formatted with augmentedImageDatastore function in Matlab to create RGB images from grayscale, crop and separate data for training. Classification algorithms were compared using pre-trained CNNs with transfer learning to test our ability to classify vasculature images as the correct organ. We used NasNetLarge, Inceptionv3, ResNet101, MobileNetv2, and GoogLeNet, all of which were pre-trained on ImageNet, a database containing more than a million images. However, using these algorithms without training on this specific dataset yields poor results (data not shown). Transfer learning allowed use of CNNs with a predetermined architecture and initialized with pre-identified parameters and features common to ImageNet to apply to our dataset, with a few adjustments.

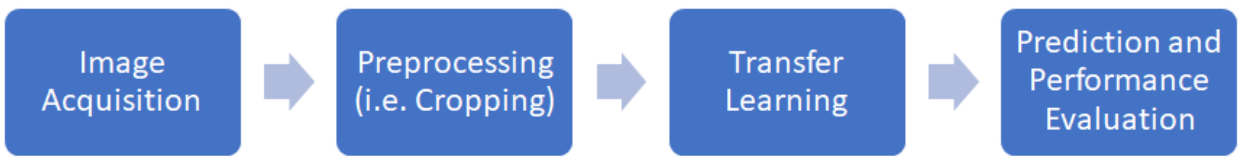

Software Flowchart:

FIJI (version 1.52p, NIH, Bethesda, Maryland)

Inputs: Light-sheet microscopy images of whole, cleared intact organs with vasculature fluorescently labeled.

Outputs: Cropped ROIs of vasculature regions separated into 1 slice per file.

Matlab (2019b, Mathworks):

Inputs: FIJI output images of ROIs from various organs

Outputs: ML technique training, testing and validation data.

Apps: Deep Network Designer (DND)

Inputs: imported pre-trained CNN classification algorithm

Outputs: modified network specified to intake vascular images with 6 classifications

Code: Two scripts to train and test/visualize

1. Train the custom CNN produced with DND
    1. Input: custom CNN network
    2. Output: trained CNN network on provided images
2. Test trained network and display predictive results
1. Input: trained CNN network on provided images
2. Output: 4 image examples with predicted class and prediction probability, a confusion matrix, test accuracy.

Transfer Learning: Matlab's Deep Network Designer was used to import the pretrained network for modification. The last fully connected layer was then removed and replaced with a fully connected layer. The new layer had a higher learning rate and our specific number of classes (six classes: brain, kidney, uterus, lymph, heart, bladder). Table 3 summarizes some of the primary differences between each of the networks. In general, the more layers and parameters, and the larger the image input size, the more accurate the network can be, but also slower (Table 3).

Network	**Depth**	**Size**	**Parameters (Millions)**	**Image Input Size**
GoogLeNet	22	27 MB	7.0	224-by-224
MobileNet-v2	53	13 MB	3.5	224-by-224
ResNet-101	101	167 MB	44.6	224-by-224
Inception-v3	48	89 MB	23.9	299-by-299
NASNet-Large	(Not linear)	360 MB	88.9	331-by-331

Table 3: Comparing Convolutional Neural network properties and image input capacity.

Each of the CNNs chosen are at the Pareto frontier, shown in the figure below (Methods Figure 5). This frontier represents the networks which can give the highest accuracy, given their relative prediction times. For example, NASNet-Large is the most accurate network given longer time. However, GoogLeNet might be a better choice if a rapid response is desired.[36]

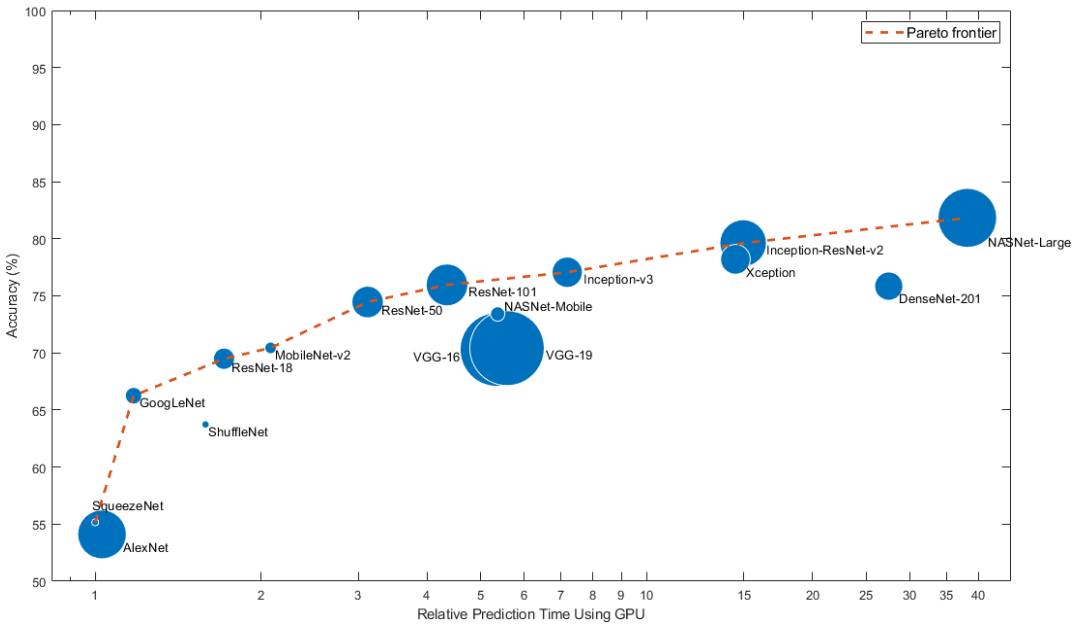

Methods Figure 5: Visualizing the efficiency of CNN algorithms by comparing time cost and accuracy, adapted from Catani, 2020. [36]

RESULTS

Lectin-Dylight-649 labels vasculature with high contrast-to-background ratio (CBR). To further evaluate the labeling capacity of perfused Lectin-Dylight-649, we compared its CBR to the Tie2-GFP transgenic vascular model. We measured fluorescence intensities of vascular and background perivascular ROIs for each fluorophore in the same region of dual-labeled brain

slices using confocal microscopy (n=4 samples) (Results Fig. 1 A-D). Vascular intensity values were shown to be higher with Lectin-Dylight-649, while background intensity values were higher for Tie2-GFP fluorescence (n=100 ROIs each) (Results Fig. 1E). In the GFP emission images, the mean fluorescence intensity was the same for the selected vascular and background ROIs (p=0.44). For all other comparisons, the mean fluorescence intensities were not equal ($p < 0.001$) (Results Fig. 2E). The measured fluorescence CBR of Tie2-GFP is ~18 times lower than that of Lectin-Dylight-649 (Results Fig. 2F). Collectively, these data demonstrate improved vascular visibility with the use of Lectin-Dylight-649 over endogenous GFP, in combination with iDISCO+ optical clearing.

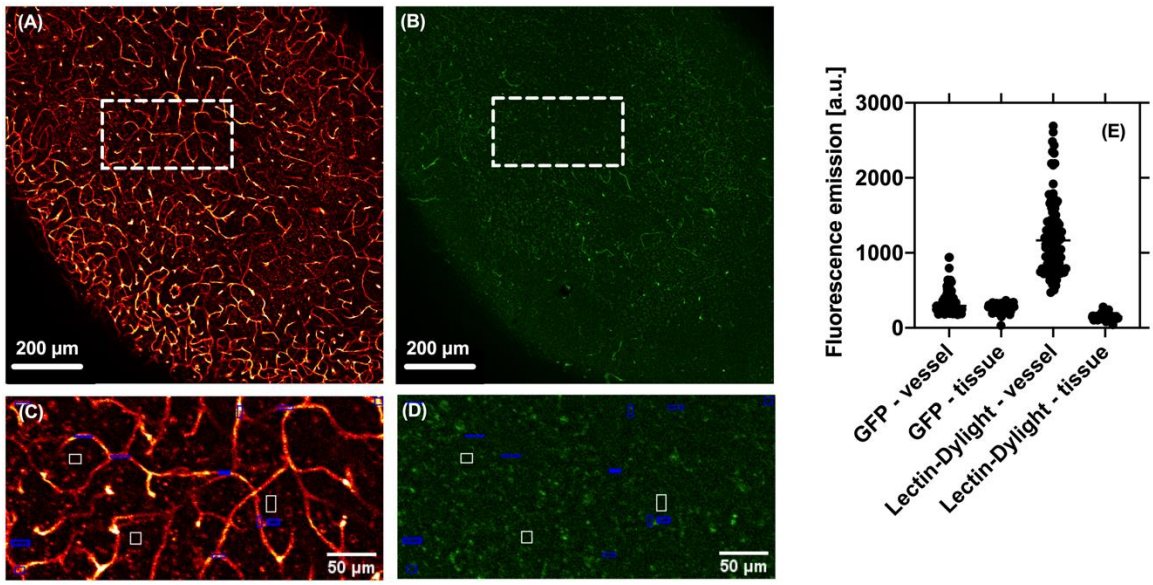

Results Figure 1: With iDISCO+ optical clearing, Lectin-Dylight-649 labeling exhibits an ~18-fold higher CBR than Tie2-GFP. (A,B) Lectin and Tie2-GFP fluorescence confocal images, respectively, shown as MIPs taken from the same region of the brain. (C,D) Representative ROIs of taken from (A,B) in perivascular (white) and vascular (blue) regions. (E) Comparison of Lectin and Tie2-GFP intensity profiles in vascular and perivascular regions (n=100 ROIs each). Mean GFP fluorescence intensities in the vascular and tissue regions were similar (p=0.44). All other comparisons had different mean intensity values ($p<0.001$).

Light sheet microscopy and modified idisco+ clearing protocol enables visiblity of lectin labeled microvasculature in slices. With the goal of imaging the whole intact brain, we first assessed the capacity of LSM to replace confocal microscopy in visualizing vessel structure with a modified iDISCO+ clearing protocol in 1mm brain sections. To test the LSM's ability to resolve vascular characteristics sufficiently, we imaged cleared ~1mm slices of Lectin perfused mouse brain (Results Fig. 2A). MIPs from the LSM (Results Fig. 3B) and 10x higher resolution confocal airyscan (Results Fig. 2C) were compared. Vascular density, as a percent of image area, was 45.3% and 45.44%, while vascular length, a skeletonized measure of vascular distance, was 4.417% and 4.219% for the airyscan and LSM respectively. A percent difference comparison between airyscan and LSM yielded 0.16% difference in density and 2.29% in length (Results Fig. 2D). Vascular density and vascular length varied by less than 3% between confocal and light sheet microscopy of lectin labeld brain slices under our modified iDISCO+ protocol.

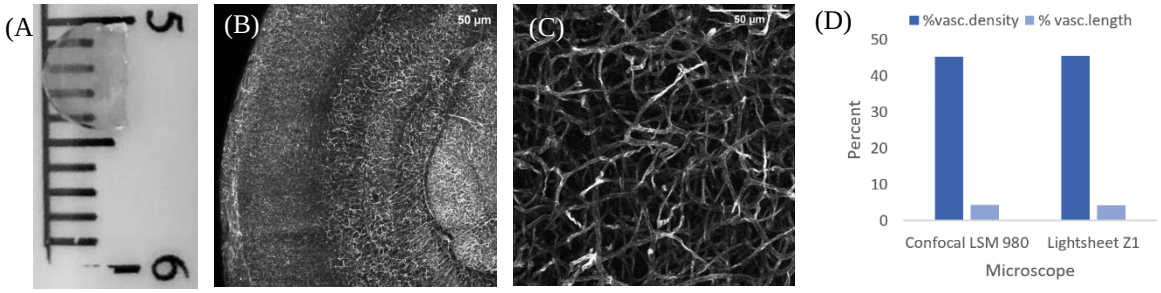

Results Figure 2: LSM enables micron resolution of Lectin labeled microvasculature in slices cleared with modified iDISCO+ protocol. (A) ~1mm cleared brain slice. (B) Light sheet MIP of 2188 x 2188-micron ROI, 1.14 micron lateral and 6.59-micron axial resolution (C) Airyscan LSM 980 MIP of 176x176 micron ROI 0.1-micron lateral resolution 0.15-micron axial resolution. (D) Comparison of vascular density and length relative to microscope used.

Whole-brain cerebral microvascular imaging in the intact brain. To visualize whole brain microvasculature, Lectin-Dylight-649 was administered via retro-orbital injection followed by cardiac perfusion and the modified iDISCO+ protocol on intact excised mouse brains. The modified iDISCO+ protocol considerably increased the transparency of the intact brain (Results Fig. 3A). LSM microscopy yielded several tiles, which were stitched and rendered in three dimensions while maintaining μm resolution over the cm-scale organ. Three-dimensional visualization depicts the detailed cerebrovascular structure (Results Fig. 3B,C). Inspection of 200 μm MIPs revealed high-resolution visibility of the vasculature throughout the brain, including internal sections (Results Fig. 3D-F).

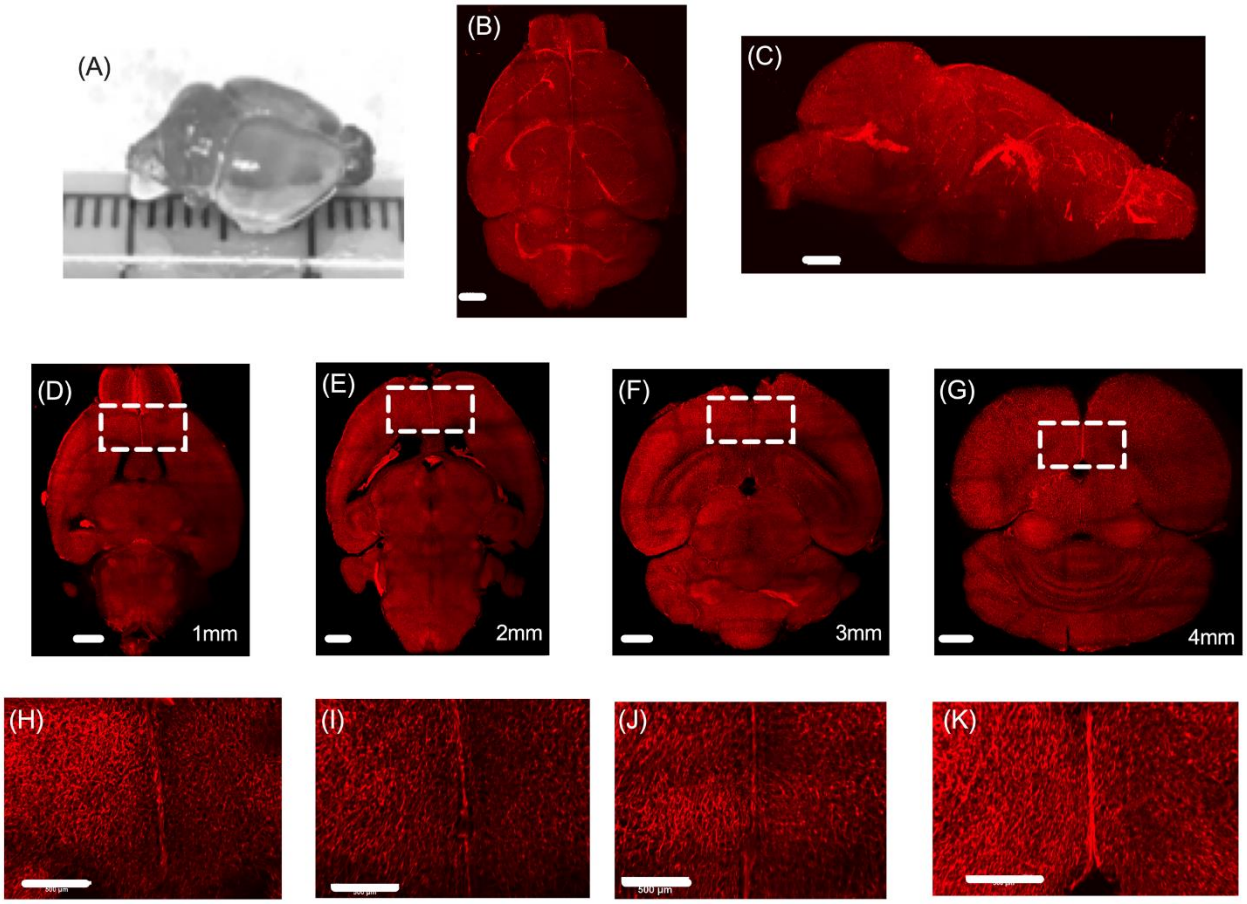

Results Figure 3: Three-dimensional whole-brain images allow dynamic structure analysis from micrometer to centimeter scales. (A) The entire brain cleared with modified iDISCO+. (B,C) Renderings of the cerebrovasculature (B) top view, (C) sagittal view. (D-G) 200 µm thick MIPs of transverse virtual sections taken in steps of 1 mm through the brain. (H-K) Magnified view outlined in (D) (scale bar 500 µm). Scale bar in all images = 500 µm

Micro-hemorrhage and vascular co-localization in 3D Brain Tissue. To quantify vascular structure in the region of microbleeds, brains cleared with modified iDisco+ protocol were imaged intact (Results Fig. 4A) and by thick, 1mm hemisphere slices (Results Fig. 4B). Several tiles were collected and stitched with confocal microscopy (Results Fig. 4C) , and each tile was assessed for microbleed burden in the 3D space over 1 mm depth (Results Fig. 4D). Vasculature was traced to extract 3D coordinates and vascular width throughout the slice to assess structure and distance to microbleeds (Results Fig. 4E-H). Colocalization of microbleeds and vasculature was done using MATLAB for each microbleed and scaled to the entire 1mm thick slice (Results Fig. 4I-L).

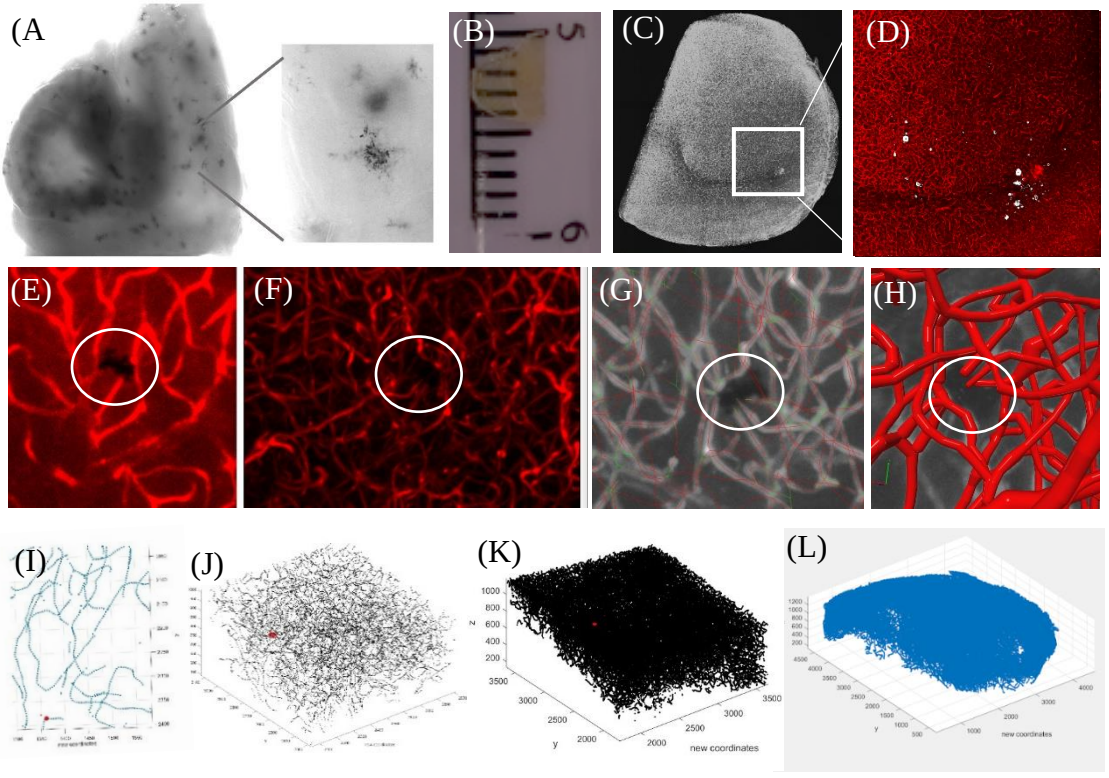

Results Figure 4: Clearing and staining with Prussian Blue dye allows for visualization of hemosiderin deposits in whole and thick-sliced brain tissue. (A) Brightfield of 3D-intact brain with Magnified ROI of microbleed location and 3D-shape. (B) 1mm thick brain hemisphere slice. (C) MIP of stitched 1mm thick slice and one tile magnification with marked microbleeds in white. (E-H) Microbleed identification and vascular tracing of (C), (E) one slice containing microbleeds highlighted in white using a FIJI processing algorithm, (F) MIP including slice from (E), (G) vascular tracing magnified MIP (H) filled in microvessels surrounding microbleed traced with software. (I-L) Computerization of vascular data surrounding microbleeds (I) dot collapsed representation microbleed location, (J) 3D volume microbleed and vascular environment (K) one tile vascular representation (L) whole stitched 3D vasculature of 1mm brain hemisphere from (C).

Machine Learning Experiment 1: Comparison of two CNNs with first data version (uncropped)

Nasnet and Inceptionv3 were adapted with transfer learning and with the first data version. As the images were augmented in the CNN's input layer, they became cropped removing valuable data and sometimes leaving blank images. Despite this, Nasnet showed accuracy at ~70%. Inceptionv3, however, performed less well at ~ 45% and prompted procession to the second version of data (Fig. 5).

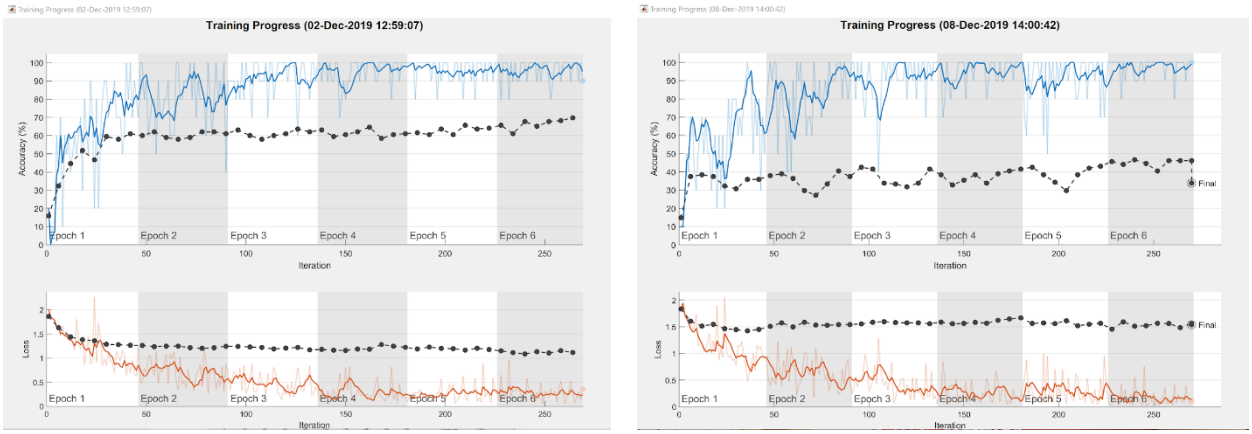

Results Figure 5: Comparison of Two CNN methodologies on first unprocessed data set. (left) Nasnet Transfer learning CNN accuracy nears 70%. (right) Inceptionv3 transfer learning shows ~45% accuracy

Machine Learning Experiment 2: Comparing CNN performance on the second data version (cropped)

Data was cropped to useful ROIs using FIJI to restack the separated slices using the Bio-formats importer. The stack was cropped with a visually chosen vascular ROI. In some instances, several ROIs from one image were used. The stacks were re-exported as separate tiffs using the Bioformats Exporter.

All pre-trained CNNs were augmented with transfer learning as listed in the Technical Approach Section. Inceptionv3 was first to train, validate and test the data. With the new, pre-processed data, results were improved: accuracy ~ 80% (Results Fig. 4). Test accuracy was 72%, as the mean of the predicted values matching validation labels. A classification Matrix reveals the challenging classifications for the CNN. Uterus is commonly misidentified as bladder, but the reverse is not true. Brain is entirely misidentified as bladder, heart and uterus, while bladder reflects this misidentification with brain, heart and uterus do not (Results Fig. 4).

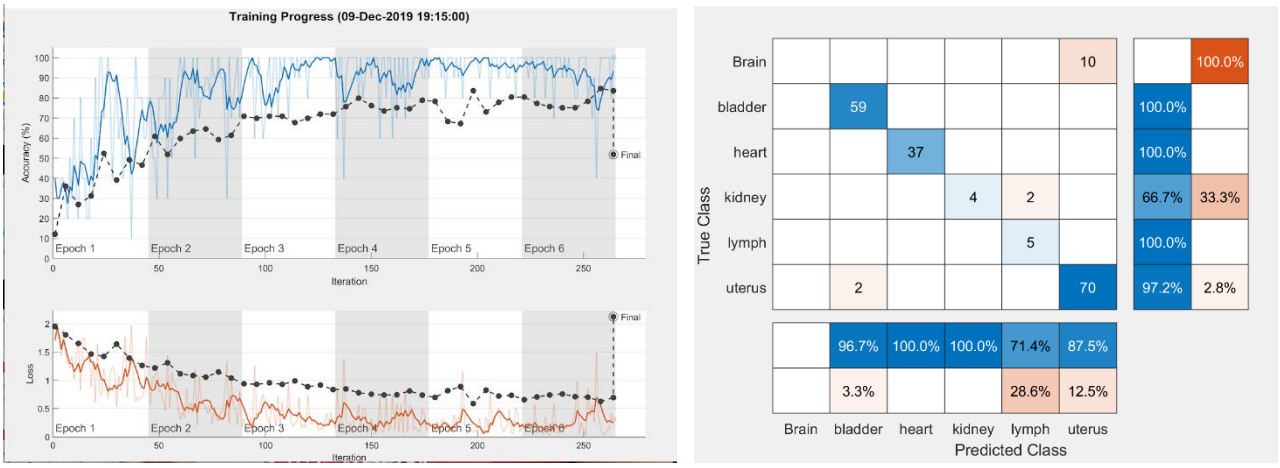

Results Figure 6: Results of Inceptionv3 algorithm on cropped data (left) training progress (right) example images with prediction probabilities.

Next, GoogLeNet was used on the same set of preprocessed data (cropped). The performance was substantially better, with a validation accuracy of 90.48% (Results Fig. 7L). In testing the trained CNN with the validation images, we see an increase in predictive probability, but test accuracy is reported at 71%.

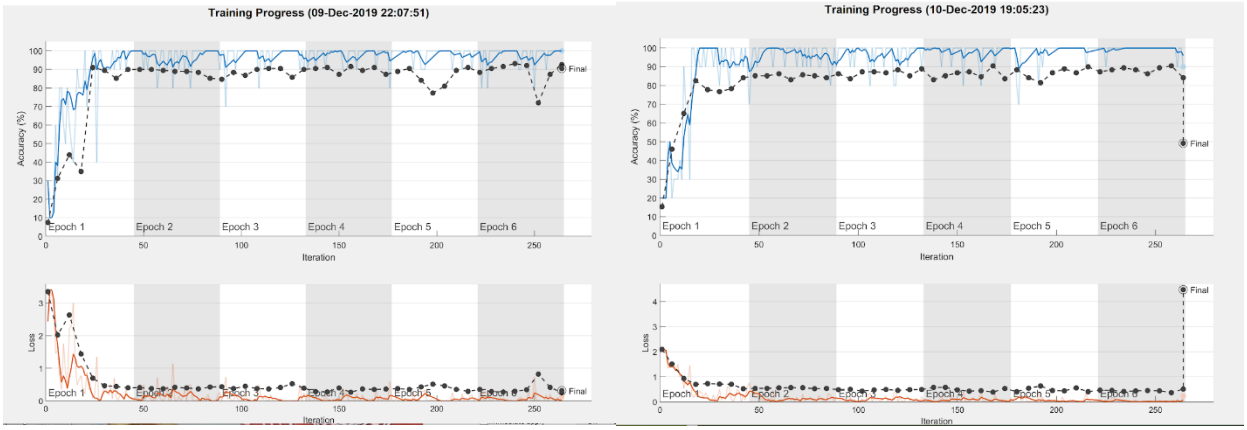

Figure 7: GoogLeNet and ResNet increase performance over Inceptionv3: (L) GoogLeNet (R) ResNet.

Similarly, using ResNet, we achieved a validation error of ~84% (approximated due to graphics error on last data point in Matlab). Test error was 71.43%. MobileNetv2 achieved a validation accuracy of ~86%. Comparing all the tested CNNs provided a comparison of validation accuracy and time (Results Fig. 8).

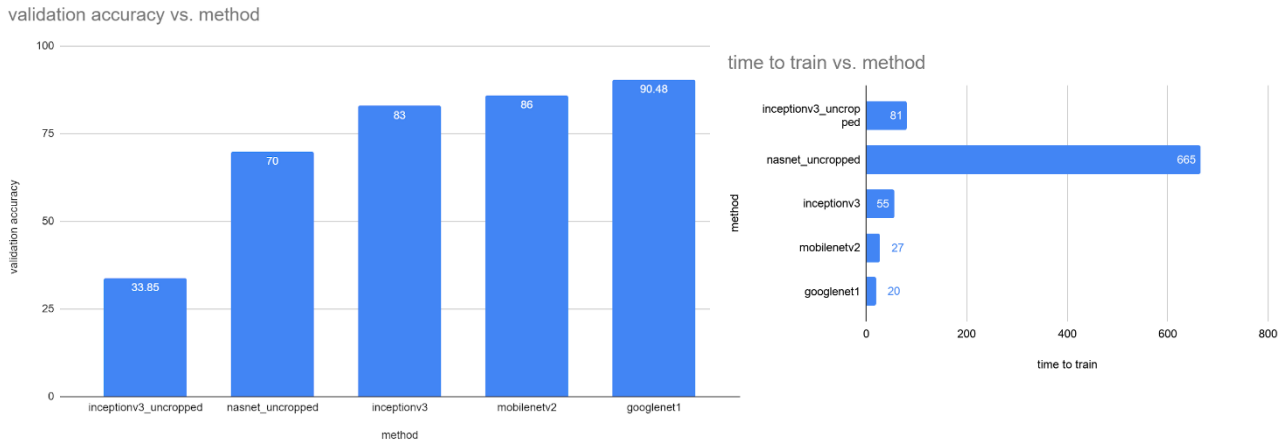

Results Figure 8: Comparison of CNN architectures for validation accuracy and time for training: (L) showing GoogLeNet has highest validation accuracy. (R) GoogLeNet has the lowest time to train (in minutes).

Machine Learning Experiment 3: Validation sensitivity to variability in data amounts

To test the malleability of the CNN's accuracy, we assessed the effect of adding 417 brain slices to the cropped data. The hypothesis before the experiment was that this would increase the training capacity of brain vasculature, decreasing misclassification error. However, the increased sample size of only brain resulted in a lower overall accuracy (93.65% to 73.97%), although brain classification was much higher (0% to 98.5%)(Results Fig. 9) .

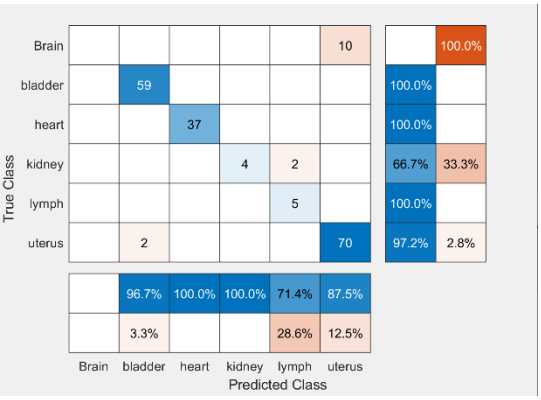

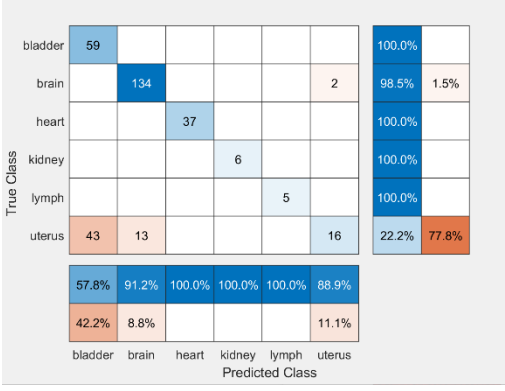

Results Figure 9: Comparing pre and post addition of brain data using GoogLeNet on cropped data (L) original "image2" data set (R) supplemented data set "Image3"

Machine Learning Experiment 4: Effects of Learning rate variation on accuracy

Because obtaining a global maximum for accuracy is not guaranteed with gradient descent, it is important to utilize learning rates which balance convergence and divergence to obtain at least a local maxima and have an idea about whether that maxima is local or global. To do this, learning rate was adjusted above and below the standard 1e-4 rate and plotted against validation accuracy. Additionally, assessing the chart of the fastest learning rate allowed us to observe the landscape of accuracies showing 80% as a high.

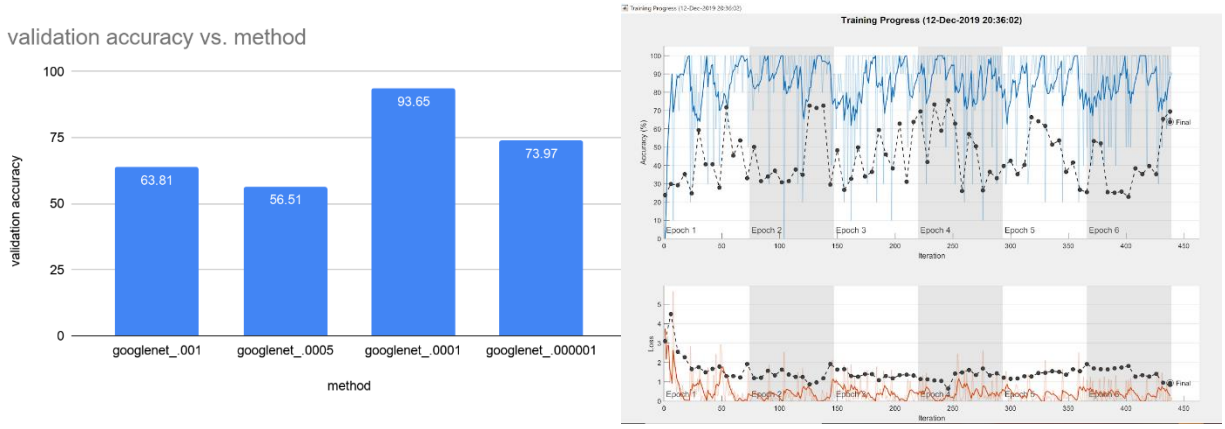

Results Figure 10: Learning rate variation shows local maxima for validation accuracy and prediction as global maxima. (L) Comparison of learning rates for GoogLeNet versus validation accuracy (R) .001 learning rate landscape showing no high maxima.

DISCUSSION

Here, we created a simple method to enable visualization of the cerebral microvasculature in an intact mouse brain with micrometer resolution. We found Lectin-Dylight-649, which is reported to be more stable than the FITC derivatives[15,16], to be an effective method for labeling blood vessels. Our data demonstrate that Lectin-Dylight-649, coupled with a modified iDISCO+ protocol for clearing, achieves superior CBR as compared with endogenous GFP in transgenic Tie2-GFP mice. Preparation of Lectin-Dylight-649 and administration into the bloodstream via retro-orbital injection both are techniques that are simple to master. Thus, our method for vessel labeling should be easy to integrate into studies with other mouse models. As a proof of concept, we demonstrated the viability of imaging cerebral microhemmorages cardio microvasculature for pathological interrogation.

We demonstrated whole-brain imaging and rendering of the cerebral microvasculature is possible with a two-day protocol. We found that using a lectin-based labeling technique and adaptation of the iDISCO+ methodology allowed for a chemically compatible protocol that was achievable in two days. Antibody-based labeling techniques can take ~one week to complete due to the need to wait for the diffusion of the antibodies and labels from the solution into the tissue sample. The required time can be reduced with the use of tissue sectioning, but with an associated loss of connectivity of features within the individual sections.

Whole-brain vascular visualization was recently demonstrated, as well as the ability to see vasculature in other organs[25,26,28]. To achieve such results, groups used complicated clearing procedures necessitating lengthy labeling techniques (~weeks) and non-standard equipment (e.g.,

Electrophoretic Tissue-Clearing chambers and hydrogel embedding equipment), which may impede the routine use of these methods for scientific research[11,17]. Our group and others have used cardiac perfusion to administer DiI as a vessel painting agent[14,37,8]. However, recent work by Salehi et al.[38] suggests that adjuvant methods (i.e., sodium nitroprusside) to dilate the vasculature is required for DiI to label the vasculature robustly. Our previous data[35] and data presented here demonstrate that Lectin-Dylight-649 enters the circulatory system via retro-orbital injection and can label vasculature while the animal is alive. We postulate that this *in vivo* vessel labeling approach is a much more straightforward and more effective approach for vessel painting.

The first application presented here exhibits the cross compatibility of this methodology with standard computational image analysis programs. The microbleed vascular co-localization pipeline provides a technique to identify vascular environments clearly and a platform to compare microbleed and vascular characteristics across pathologies. With the compressed data format of extracted coordinates and volume, mathematical concepts are easily applied in a programming atmosphere.

The second application to cardiovasculature attests to the extension of this process beyond cerebrovasculature. This methodology may be a viable construct for the investigation of cardio microvascular disease, given its compatibility with co-labels and unaltered, whole-organ perspective with micron detail.

Although the present study describes a translatable protocol for vascular labeling, we did not test the compatibility and visibility of other labels, including fluorophore-conjugated antibodies, with our optical clearing protocol. For example, our previous work centered on FocusClear-based optical clearing has included the use of nuclear stains (i.e., DAPI), fibrillar beta-amyloid (Thioflavin S) and hemosiderin labels (Prussian Blue)[8,39]. Also, previous work demonstrates that organic solvent-based approaches may quench endogenous fluorescence; thus, the Tie2GFP fluorescence may have been quenched and resulted in lower CBR that we report here[40]. Future work is required to demonstrate the degree to which fluorescence of Lectin-Dylight-649 is preserved with time.

Future work will involve systematic refinement of our clearing protocol with alternate versions of the "DISCO" protocol (e.g., FDISCO, SDISCO, UDISCO). These newer protocols are designed to increase photostability, preserve endogenous fluorescent signals, and clear the whole body[41,42,43]. Additionally, our data suggest that the vessel labeling and clearing approach can be applied to investigate both normal and abnormal vascular architecture in other organs.

Machine Learning

To this end, the machine learning experiments yielded some promising results. We were able to show the application of machine learning classification algorithms to accurately identify vasculature images of six different organ types given a single slice of ~5 μm thick data without segmentation. We showed improved results with minimal preprocessing by selecting vascular ROIs and identified GoogLeNet as the most accurate and fastest classifier for this data. Sensitivity to data amounts was shown from addition of a single data type, resulting in reduced sensitivity to other data types (Results Fig. 9). We then verified the choice of .0001 for learning

rate, for six epochs, by manipulating this value from .001 to .000001. We believe this will be useful in classifying vasculature of pathological models such as cancerous lymphatic vasculature to wildtype. Without the need for segmentation, preprocessing is minimal and holds promise for vast implementation.

Originally, NasNetLarge, rated the highest accuracy on the Pareto Frontier, was predicted to be most successful, however, due to large processing time, it only ran on uncropped data, and thus cannot be appropriately compared. Based on the second data version experiments, GoogLeNet had the highest accuracy in training and validation datasets, in addition to a fast prediction speed, completing six epochs in 20 minutes (Results Fig. 8). While we improved accuracy by cropping ROIs, a different approach would be to relabel blank images as none, in which some of the other pre-trained networks might have done better.

To improve consistency, we could decrease the training-to-testing data ratio. This would reduce the likelihood of over-fitting, which seemed to be a problem from the high validation error rate for most of the networks. Evaluating the vasculature in greater biological detail may be useful. The organs' vasculature were assumed to be sufficiently different for classification. However, based on the confusion matrices, some organs are less distinct. In the Inceptionv3 and GoogLeNet network, none of the brain images could be classified correctly as brain (Results Fig. 6&9) before the addition of more brain data.

Limitations include limited data samples, biased sampling collected by the same user and technique, inconsistent scaling. Addressing these items is expected to increase validation accuracy significantly.

Given the mathematically challenging task of characterizing vessel structures algorithmically, ML techniques may fill this gap. The success of these experiments helps characterize the complexity of vasculature networks, which is clinically relevant to identify abnormal vasculature. Following fine-tuning of this model, new experiments may include classifying vasculature by organ region and pathology.

CONCLUSION

We describe an experimental protocol to visualize the three-dimensional microvascular architecture of the intact mouse brain and its potential for extension to several pathologies. The combination of retro-orbital injection of Lectin-Dylight-649 to label the vasculature, the clearing process of a modified iDISCO+ protocol, and light-sheet imaging, collectively enables a comprehensive view of the microvasculature. Eliminating additional dehydration/rehydration steps and immersion labeling reduced clearing time to two days. It is done without the use of slicing or traditional histology methods and allows for structural information to be compacted and analyzed without loss of pertinent data. Our protocol is expected to facilitate rapid three-dimensional visualization of the microvascular network for a wide variety of biological and biomedical applications.

Additionally, we showed the capacity of this technique to label multiple organs and the opportunity to cross compare cerebrovasculature to cardiovasculature. The analysis of large data sets may be aided by the use of machine learning techniques which can decipher variable vascular structures with transfer learning techniques of convolutional neural networks.

FUTURE STUDIES

Considerable effort has been put forth in detailed studies on the brain. However, key entities such as the Allen Brain Institute and American Heart Association have described the need for studies of cerebrovascular-cardiovascular links. Here, I propose several opportunities for extending the research described here into the cardiovascular space.

Microvascular Coronary Dysfunction (MCD): Cardiovascular Disease (CV) has the highest mortality rate in the world. Non-obstructive CV, which accounts for ~30% of CV cases, has been an ill-defined disease until its recent associations to MCD in up to ⅔ of patients.[44] Deciphering the role of MCD in the onset of CV is a major objective for the development of prevention and treatment strategies, as no standard protocols currently exist.[45,46,44,47] Studies of tissue slices have yielded some useful information on ischemia-induced microvascular changes; however, whole-organ visualizations hold great promise for illuminating the dynamics underlying MCD.[45,46] 3D whole-heart computational models at the microvasculature scale have the ability to characterize the biological forces complicit in the development of MCD and inform potential treatment and prevention options.

Quantitative Characterization of Cardiac Microvasculature: 3D computerized models of the heart and brain have been developed and successfully utilized to inform new approaches to prevention and treatment (ApiNATOMY, 3D4Medical).[30,48] However, heart models do not capture the microvasculature. To develop a 3D model of the microvasculature of the heart, it will be necessary to complete a series of steps shown to be effective for visualizing dynamic

anatomical properties of human organs.[17] These steps include utilizing light sheet microscopy to yield high-resolution images of tissue samples,[17] comparing images from healthy and diseased organs,[45] and mathematically modelling the conversion of healthy microvasculature to that of a diseased organ.[49] Here we show the ability of a modified iDISCO+ clearing protocol to visualize the cardio microvasculature as an initial step towards the development of whole-heart computational microvasculature models.

Preliminary Data**.** To visualize whole heart microvasculature, Lectin-Dylight-649 was administered via retro-orbital injection followed by cardiac perfusion and the modified iDISCO+ protocol on intact excised mouse hearts. The modified iDISCO+ protocol considerably increased the transparency of the intact heart (Fig. F1A,B). LSM microscopy yielded several tiles, which were rendered in three dimensions while maintaining μm resolution over the cm-scale organ. The cardiovascular structure can be viewed in detail utilizing the modified iDISCO+ protocol with light sheet microscopy (Fig. F1 C,D).

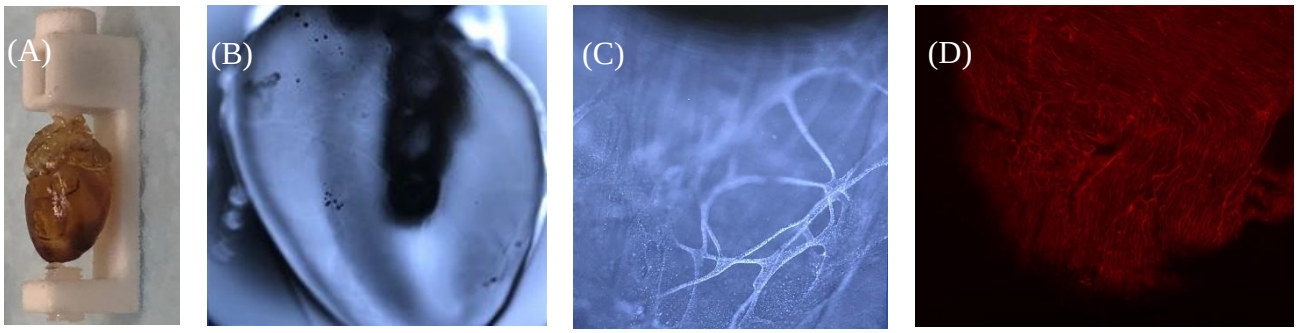

Figure F1: Three-dimensional whole-heart images allow dynamic structure analysis from micrometer to centimeter scales. (A) Entire heart cleared with modified iDISCO+ and mounting for lightsheet microscopy. (B,C) Brightfield visuals of cardiovasculature during lightsheet microscopy, (B) whole cleared heart, (C) Magnified view of microvascular structure (F) Single illuminated slice of x μm with an excitation of 638nm.

Coronary Artery Disease. As the leading global cause of death, CV kills 633,000 annually in the US, which costs ~ $200 billion a year.[50] The most common type, coronary artery disease (CAD), is classified as obstructive or non-obstructive based on clinical assessment of artery blockage. While diagnostics and clinical treatments exist for obstructive CAD, non-obstructive CAD (N-CAD) is elusive and ill-defined, accompanied by higher risk of adverse outcomes and medical costs.[9] In the past two decades, recognition of unexplained N-CAD has prompted the assessment of microvascular impact, which is not visible in humans *in vivo*.[51,47] Research has implicated microvascular coronary dysfunction (MCD) in as high as two-thirds of N-CAD cases, predominantly female (56% - 82%).[44] However, no established treatment protocol exists for MCD, due to the lack of characterization, mechanistic models and visual representations of dynamics.[45,47]

Gender Differences in MCD. As a majorly female disease, misdiagnosis of MCD has contributed to the disproportionately high burden of costs, adverse outcomes and mortality for women from heart attacks.[52] Women are nine times more likely to succumb to heart disease than breast cancer; 1 in 2.6 women will die from coronary heart disease; and 64% of women who die from heart disease had no previous symptoms.[50,53,52] The first large heart disease study to include women was in 1970, where they identified that women with a positive stress test, indicating oxygen perfusion deficiencies, were 4.5 times more likely than men to have no obstruction. From this they assumed (incorrectly) that women were less likely to get CV.[53] The federally funded Women's Ischemia Syndrome Evaluation (WISE) study was founded in 1996 to unveil the confounding factors of women's heart disease.[52] However, in 2000, 60,000 more women than men were dying from CV annually.[53]

The WISE study found that symptomatic women with clear arteries were failing vascular function tests and attested to the involvement of microvascular dysfunction. Assessment of autopsies and biomarkers supported a role of inflammation and deposition of plaque around an artery, rather than in one place as seen in men.[53] Inflammation, which causes removal of cells along the endothelial lining of blood vessels, could be increasing opportunities for the uniform plaque buildup. Hypertension also destroys the endothelial barrier and may contribute to the perpetuation of inflammatory signaling, causing small blood clots and thus heart attacks from the MCD condition.[53] Currently, the WISE study suggests anti-hypertensives and anti-inflammatories as treatment for MCD, although the etiology of this disease is not completely understood.[54]

Hypertension. Hypertension is a primary risk factor in small vessel diseases of several other organs including the brain's Microvascular Ischemic Disease, and kidneys' Chronic Kidney Disease.[55] It is hypothesized that hypertension causes microvasculature remodeling as the result of normalization forces to arterial wall stress, compensating to preserve cardiac output.[54] However, the manifestation of these changes is not clear, and depiction is expected to identify novel therapeutic targets.[46] Additionally, it has been suggested that the increase in hypertension is not linearly correlated with CV, rather it is more closely associated with a relative assessment of blood pressure according to age. Remodeling of vasculature is seen with aging, and thus assessment of hypertensive burden must include a wide age range.[54]

REFERENCES

[1] Y. Shi and J. M. Wardlaw, "Update on cerebral small vessel disease: a dynamic whole-brain disease," *Stroke Vasc. Neurol.* **1**(3), 83–92 (2016).

[2] L. W. Harris *et al.*, "The cerebral microvasculature in schizophrenia: A laser capture microdissection study," *PLoS One* **3**(12), e3964 (2008).

[3] A. F. Logsdon *et al.*, "Role of microvascular disruption in brain damage from traumatic brain injury," *Compr. Physiol.* **5**(3), 1147–1160 (2015).

[4] R. K. Sumbria *et al.*, "A murine model of inflammation-induced cerebral microbleeds," *J. Neuroinflammation*, vol. 13, no. 1, p. 218, Dec. 2016.

[5] Allison D Griffin, L Christine Turtzo, Gunjan Y Parikh, Alexander Tolpygo, Zachary Lodato, Anita D Moses, Govind Nair, Daniel P Perl, Nancy A Edwards, Bernard J Dardzinski, Regina C Armstrong, Abhik Ray-Chaudhury, Partha P Mitra, Lawrence L Latour, Traumatic microbleeds suggest vascular injury and predict disability in traumatic brain injury, Brain, Volume 142, Issue 11, November 2019, Pages 3550–3564, https://doi.org/10.1093/brain/awz290

[6] J. Epah *et al.*, "3D imaging and quantitative analysis of vascular networks: A comparison of ultramicroscopy and micro-computed tomography," *Theranostics*, vol. 8, no. 8, pp. 2117–2133, 2018.

[7] Ueda, H.R., Ertürk, A., Chung, K. et al. Tissue clearing and its applications in neuroscience. Nat Rev Neurosci 21, 61–79 (2020). https://doi.org/10.1038/s41583-019-0250-1

[8] A. J. Moy, M. P. Wiersma, and B. Choi, "Optical Histology: A Method to Visualize Microvasculature in Thick Tissue Sections of Mouse Brain," *PLoS One* **8**(1), e53753 (2013).

[9] N. Renier, Z. Wu, D. J. Simon, J. Yang, P. Ariel, and M. Tessier-Lavigne, "iDISCO: A Simple, Rapid Method to Immunolabel Large Tissue Samples for Volume Imaging," Cell, vol. 159, no. 4, pp. 896–910, Nov. 2014.

[10] Cai, R. et al. Panoptic imaging of transparent mice reveals whole-body neuronal projections and skull–meninges connections. *Nat. Neurosci.* **22**, 317–327 (2019).

[11] E. Lugo-Hernandez *et al.*, "3D visualization and quantification of microvessels in the whole ischemic mouse brain using solvent-based clearing and light sheet microscopy," *J. Cereb. Blood Flow Metab.*, **37**(10), 3355–3367 (2017).

[12] A. Ertürk, D. Lafkas, and C. Chalouni, "Imaging Cleared Intact Biological Systems at a Cellular Level by 3DISCO," *J. Vis. Exp.*, **89,** e51382 (2014).

[13] A. J. Moy, P. C. Lo, and B. Choi, "High-resolution visualization of mouse cardiac microvasculature using optical histology," *Biomed. Opt. Express* **5**(1), 69-77 (2014).

[14] A. Konno, N. Matsumoto, and S. Okazaki, "Improved vessel painting with carbocyanine dye-liposome solution for visualisation of vasculature," *Sci. Rep.*, **7**(1), 1-9 (2017).

[15] G. T. Hermanson and G. T. Hermanson, "(Strept)avidin–Biotin Systems," *Bioconjugate Techniques*, Chapter 11, 465–505, Academic Press (2013).

[16] R. T. Robertson *et al.*, "Use of labeled tomato lectin for imaging vasculature structures.," *Histochem. Cell Biol.* **143**(2), 225–234 (2015).

[17] A. P. Di Giovanna *et al.*, "Whole-Brain Vasculature Reconstruction at the Single Capillary Level," *Sci. Rep.* **8**(1), p 1-11 (2018).

[18] J. Mahmoudian et al., "Comparison of the photobleaching and photostability traits of Alexa fluor 568- and fluorescein isothiocyanate- conjugated antibody," Cell J., vol. 13, no. 3, pp. 169–172, Sep. 2011.

[19] Hama, H. et al. Scale: a chemical approach for fluorescence imaging and reconstruction of transparent mouse brain. Nat. Neurosci. 14, 1481–1488 (2011)

[20] Richardson, D. S. & Lichtman, J. W. Clarifying Tissue Clearing. Cell 162, 246–257 (2015).

[21] Murakami, T. C. et al. A three-dimensional single-cell-resolution whole-brain atlas using CUBIC-X expansion microscopy and tissue clearing. Nat. Neurosci. 21, 625–637 (2018).

[22] Tomer, R., Ye, L., Hsueh, B. & Deisseroth, K. Advanced CLARITY for rapid and high-resolution imaging of intact tissues. Nat. Protoc. 9, 1682–1697 (2014).

[23] Yang, B. et al. Single-cell phenotyping within transparent intact tissue through whole-body clearing. Cell 158, 945–958 (2014).

[24] Kim, S. Y. et al. Stochastic electrotransport selectively enhances the transport of highly electromobile molecules. Proc. Natl Acad. Sci. USA 112, E6274–E6283 (2015).

[25] K. Chung *et al*., "Structural and molecular interrogation of intact biological systems, *Nature* 497(7449), 332-337 (2013).

[26] D. Jing *et al.*, "Tissue clearing of both hard and soft tissue organs with the pegasos method," *Cell Res.* 28(8), 803–818 (2018).

[27] Zeiss, “Light Sheet Microscopy LSFM for Large Living Samples - Light sheet Z.1.” [Online]. Available: https://www.zeiss.com/microscopy/us/products/imaging-systems/light sheet-z-1.html. [Accessed: 08-Jul-2019].

[28] C. M. França *et al.*, “3D-Imaging of Whole Neuronal and Vascular Networks of the Human Dental Pulp via CLARITY and Light Sheet Microscopy,” *Sci. Rep.,* **9(**1), 1-10 (2019).

[29] “3D4Medical – Award-winning 3D Anatomy and Medical Apps.” [Online]. Available: https://3d4medical.com/. [Accessed: 13-Dec-2018].

[30] “ApiNATOMY | Biological Visualisation Community.” [Online]. Available: https://bivi.co/visualisation/apinatomy. [Accessed: 13-Dec-2018].

[31] I. D. Kelch, G. Bogle, G. B. Sands, A. R. J. Phillips, I. J. LeGrice, and P. Rod Dunbar, “Organ-wide 3D-imaging and topological analysis of the continuous microvascular network in a murine lymph node,” Sci. Rep., vol. 5, no. 1, p. 16534, Dec. 2015.

[32] Badawi, Sufian & Fraz, Muhammad. (2019). Multiloss Function Based Deep Convolutional Neural Network for Segmentation of Retinal Vasculature into Arterioles and Venules. BioMed Research International. 2019. 1-17. 10.1155/2019/4747230.

[33] Haft-Javaherian M, Fang L, Muse V, Schaffer CB, Nishimura N, Sabuncu MR (2019) Deep convolutional neural networks for segmenting 3D in vivo multiphoton images of vasculature in Alzheimer disease mouse models. PLoS ONE 14(3): e0213539. https://doi.org/ 10.1371/journal.pone.0213539

[34] J. C. Montoya, Y. Li, C. Strother, and G. H. Chen, “3D deep learning angiography (3D-DLA) from C-arm Conebeam CT,” *Am. J. Neuroradiol.*, vol. 39, no. 5, pp. 916–922, May 2018.

[35] M. Loren *et al.*, "Optical clearing potential of immersion-based agents applied to thick mouse brain sections," *PloS One* 14(5), e0216064 (2019).

[36] Catani, Filippo. (2020). Landslide detection by deep learning of non-nadiral and crowdsourced optical images. Landslides. 10.1007/s10346-020-01513-4.

[37] Y. Li, Y. Song, L. Zhao, G. Gaidosh, A. M. Laties, and R. Wen, “Direct labeling and visualization of blood vessels with lipophilic carbocyanine dye DiI,” Nat. Protoc., vol. 3, no. 11, pp. 1703–1708, 2008.

[38] A. Salehi *et al.*, “Novel Technique for Visualizing and Analyzing the Cerebral Vasculature in Rodents,” *Transl Stroke Res* 10(2), 216-230 (2019).

[39] P. Lo *et al.*, “Visualization of microbleeds with optical histology in mouse model of cerebral amyloid angiopathy,” *Microvasc Res* 105, 109–113 (2016).

[40] G. Elliott and P. O'Hare, "Intercellular trafficking of VP22-GFP fusion proteins," *Gene Ther* 6(1), 149–151 (1999).

[41] C. Hahn *et al.*, "High-resolution imaging of fluorescent whole mouse brains using stabilised organic media (sDISCO)," *J. Biophotonics* **12**(8), e201800368 (2019).

[42] C. Pan *et al.*, "Shrinkage-mediated imaging of entire organs and organisms using uDISCO," *Nat. Methods* **13**(10), 859–867 (2016).

[43] Y. Qi *et al.*, "FDISCO: Advanced solvent-based clearing method for imaging whole organs," *Sci Adv* **5**(1), eaau8355 (2019).

[44] A. Alrifai, M. Kabach, J. Nieves, J. Pino, and R. Chait, "Microvascular Coronary Artery Disease: Review Article," US Cardiol. Rev., p. 1, 2017.

[45] P. Gkontra, K.-A. Norton, M. M. Żak, C. Clemente, J. Agüero, B. Ibáñez, A. Santos, A. S. Popel, and A. G. Arroyo, "Deciphering microvascular changes after myocardial infarction through 3D fully automated image analysis," Sci. Rep., vol. 8, no. 1, p. 1854, Dec. 2018.

[46] M.-Q. Zhang, L. Zhou, Q.-F. Deng, Y.-Y. Xie, T.-Q. Xiao, Y.-Z. Cao, J.-W. Zhang, X.-M. Chen, X.-Z. Yin, and B. Xiao, "Ultra-high-resolution 3D digitalized imaging of the cerebral angioarchitecture in rats using synchrotron radiation," Sci. Rep., vol. 5, p. 14982, Oct. 2015.

[47] J. W. Petersen and C. J. Pepine, "Microvascular coronary dysfunction and ischemic heart disease: where are we in 2014?," Trends Cardiovasc. Med., vol. 25, no. 2, pp. 98–103, Feb. 2015.

[48] P. Causin and F. Malgaroli, "Mathematical modeling of local perfusion in large distensible microvascular networks," Comput. Methods Appl. Mech. Eng., vol. 323, pp. 303–329, Aug. 2017.

[49] L. W. Harris *et al.*, "The cerebral microvasculature in schizophrenia: A laser capture microdissection study," *PLoS One* **3**(12), e3964 (2008).

[50] "Women and Heart Disease Fact Sheet|Data & Statistics|DHDSP|CDC." [Online]. https://www.cdc.gov/dhdsp/data_statistics/fact_sheets/fs_women_heart.htm.

[51] P. G. Camici, G. d'Amati, and O. Rimoldi, "Coronary microvascular dysfunction: mechanisms and functional assessment," Nat. Rev. Cardiol., vol. 12, no. 1, pp. 48–62, Jan. 2015.

[52] L. J. Shaw, R. Bugiardini, and C. N. B. Merz, "Women and ischemic heart disease: evolving knowledge.," J. Am. Coll. Cardiol., vol. 54, no. 17, pp. 1561–75, Oct. 2009.

[53] “New view of heart disease in women - Harvard Health.” [Online]. Available: https://www.health.harvard.edu/staying-healthy/new-view-of-heart-disease-in-women. [Accessed: 13-Dec-2018].

[54] J. Mayet and A. Hughes, “Cardiac and vascular pathophysiology in hypertension.,” Heart, vol. 89, no. 9, pp. 1104–9, Sep. 2003.

[55] M. Kanbay, L.-G. Sanchez-Lozada, M. Franco, M. Madero, Y. Solak, B. Rodriguez-Iturbe, A. Covic, and R. J. Johnson, “Microvascular disease and its role in the brain and cardiovascular system: a potential role for uric acid as a cardiorenal toxin,” Nephrol. Dial. Transplant., vol. 26, no. 2, pp. 430–437, Feb. 2011.

SUPPLEMENTAL VIDEOS

Supplemental Video 1: Fly-through rendering of 2.2 mm of intact, cleared brain with vasculature labeled with Lectin-Dylight-649. Images collected with the Zeiss Z.1 light-sheet microscope. Imaris software was used to render the data set.

Supplemental Video 2: Stitched fly-through rendering of 3.9 mm of an intact, cleared brain labeled with Lectin-Dylight-649. Lightsheet microscope was used with dual-side fusion and pivot scanning to equalize emissions across the whole brain and reduce shadowing effects, respectively. Imaris software was used to stitch and render a 4x3 array of tiles. Total volume size is 31.6mm x 23.6 mm x 3.9 mm.

Supplemental video 3: Fly-through video of microvascular structures co-localized with microbleed labeling in 3D from 1mm sliced cleared brain labeled with Lectin-Dylight-649. Confocal microscopy was used at two separate emissions to gather and dual project the resulting images. FIJI was used to create the video.